

Emission of intermediate mass fragments from hot $^{116}\text{Ba}^*$ formed in low-energy $^{58}\text{Ni}+^{58}\text{Ni}$ reaction

M. Balasubramaniam, Rajesh Kumar and Raj K. Gupta
Physics Department, Panjab University, Chandigarh-160014, India.

C. Beck

*Institut de Recherches Subatomiques, UMR7500, IN2P3/ Université
Louis Pasteur, B.P. 28, F-67037 Strasbourg Cedex 2, France.*

Werner Scheid

*Institut für Theoretische Physik, Justus-Liebig-Universität,
Heinrich-Buff-Ring 16, D-35392, Giessen, Germany.*

November 19, 2018

Abstract

The complex fragments (or intermediate mass fragments) observed in the low-energy $^{58}\text{Ni}+^{58}\text{Ni}\rightarrow^{116}\text{Ba}^*$ reaction, are studied within the dynamical cluster decay model for s-wave with the use of the temperature-dependent liquid drop, Coulomb and proximity energies. The important result is that, due to the temperature effects in liquid drop energy, the explicit preference for α -like fragments is washed out, though the ^{12}C (or the complementary ^{104}Sn) decay is still predicted to be one of the most probable α -nucleus decay for this reaction. The production rates for non- α like intermediate mass fragments (IMFs) are now higher and the light particle production is shown to accompany the IMFs at all incident energies, without involving any statistical evaporation process in the model. The comparisons between the experimental data and the (s-wave) calculations for IMFs production cross sections are rather satisfactory and the contributions from other ℓ -waves need to be added for a further improvement of these comparisons and for calculations of the total kinetic energies of fragments.

Pacs No. 25.70.Jj, 23.60.+e, 23.70.+j, 24.10.-i

1 INTRODUCTION

In low-energy heavy-ion reactions, intermediate mass fragments (IMFs) i.e. complex fragments with masses lighter than $A < 20$, are emitted from both the light ($A \sim 60$) and medium-mass ($A \sim 110$) compound systems, and may arise as multiple "clusters", and are accompanied by multiple light particles ($Z \leq 2$) production. This light-particle emission, associated with evaporation residues production, is very satisfactorily understood as the fusion-evaporation process from an equilibrated compound nucleus in the statistical Hauser-Feshbach formalism [1, 2, 3, 4, 5], described in evaporation codes such as LILITA and CASCADE or many other codes. The Hauser-Feshbach formalism has been extended to include the above noted observed complex IMFs, for example in the BUSCO code [2] or in the Extended Hauser-Feshbach Method based on the scission-point picture [5]. An alternative process for the IMFs production is the binary decay of a compound nucleus in the statistical fission model of Moretto [6] or of Vandenbosch and Huizenga [7]. The fission model of [6] is used in the GEMINI code [1] for the heavier compound systems ($A > 100$), whereas the saddle-point transition-state model based on fission model of [7] is used for the lighter systems ($A < 80$) [4]. The emission of light particles (n, p, α or γ -ray) in both of these fission models is still calculated within the Hauser-Feshbach formalism [8].

We know that the fission and cluster-decay are competing processes with the latter being more prevalent for lighter fragments [9]. In view of this result, in a very recent paper [10], we have proposed for the first time an alternative new "cluster decay" process for the IMFs emitted from an excited $^{116}\text{Ba}^*$ compound nucleus produced in the low-energy $^{58}\text{Ni} + ^{58}\text{Ni}$ reaction. The IMFs are shown to arise as multiple "clusters" of masses $A < 20$, and only at $E_{lab} > 200$ MeV, in agreement with experimental results of Beckerman et al. [11]. This result has its origin in the macroscopic liquid drop energy, since the shell effects are almost zero at the excitation energies involved. The multiple light particle ($Z \leq 2$) emission, other than via the statistical evaporation process (not treated in this model), is also shown to become equally probable at higher energies where only the pure liquid drop energies enter the calculations. The macroscopic liquid drop energy was, however, taken to be temperature-independent [10] and only the angular momentum $\ell = 0$ case was considered. Also, a generalized liquid-drop model has been proposed recently by Royer and Moustabchir [12] to describe the light-nucleus emission.

In this paper, we extend our previous work [10] by using the temperature-dependent liquid drop energy ($V_{LDM}(T)$) from Davidson et al. [13], since the compound nucleus is hot enough at the excitation energies of interest. The other terms of the potential, that constitute the scattering potential $V(R)$, are also taken temperature-dependent, based on Refs. [13, 14]. In other words, we use a complete temperature-dependent potential and apply it to the medium-mass, hot compound system $^{116}\text{Ba}^*$ formed in $^{58}\text{Ni} + ^{58}\text{Ni}$ reaction at various (low) incident energies [2, 15, 16, 17]. Also, some of the specific data [2, 15] chosen here, and discussed in the following paragraph, was not analysed in our earlier work [10]. This system has been of much interest from the point of view

of the exotic ^{12}C (or ^{100}Sn) cluster radioactivity [17, 18, 19, 20, 21], first expected as a ground-state decay [18, 19, 20, 21], but now seems to have observable yields only for the decay of the corresponding excited compound system [17]. Another important point to note is that ^{116}Ba is mainly a positive Q -value (Q_{out}) system (negative Q_{out} only for some light decay-fragments). Our model is also applied to a negative Q_{out} , light compound system ^{56}Ni [22]. Also, the other, both lighter and heavier, isotopes of barium, $^{112-120,126}\text{Ba}$, have been of interest for both the ground-state and excited state decay studies [18, 23].

The data chosen to test our model calculations in the following are the IMFs production cross sections, measured in (i) the 630 MeV $^{58}\text{Ni}+^{58}\text{Ni}\rightarrow^{116}\text{Ba}^*$ reaction [2, 15], whose kinematical analysis of fragments (the similarity of Gaussian shaped energy spectra of fragments in coincidence with γ rays, and the flat angular distribution of their ground and excited states) revealed that the IMFs with $4\leq Z\leq 9$ are consistent with the decay of a compound nucleus formed in a complete fusion reaction and that the effective temperature of the emitting system, estimated on the basis of a simple statistical approach for primary fragments, is on the average about 2.2 MeV, which is about half of the compound nucleus temperature T ($=4.42$ MeV, based on Eq. (13) below); and (ii) the 348, 371 and 394 MeV $^{58}\text{Ni}+^{58}\text{Ni}$ reaction [17], where the pure Hauser-Feshbach BUSCO predictions do not match the measured cross sections (the same code is used with a reasonable success for the above mentioned data at 630 MeV [2, 15]). In other words, so far only the pure Hauser-Feshbach analysis is made for both the experiments. Also, like in [2, 15], the total excitation energy (TXE) in the exit channel is observed to be too small (~ 50 MeV), compared to the available compound nucleus excitation energy E_{CN}^* ($=96.4$ to 130.9 MeV). As is already discussed in our earlier work [10], such data on TXE (or TKE) are best treated in a fission or a cluster decay model, and we use here the cluster decay model.

The dynamical cluster-decay model for hot compound systems, a reformulation of the preformed cluster model (PCM) of Gupta and collaborators [24, 25, 26, 27, 28] for ground-state decays, is presented in Sec. 2 and its application to the hot $^{116}\text{Ba}^*$ nucleus data is made in Sec. 3. The experimental data for IMFs production cross sections are taken from Fig. 6 of [2], and from Table 1 or Fig. 2 of [17]. It may be noted that any discussion of the emitted light particles in this paper is of those predicted here to occur at higher energies, and for the $\ell=0$ case only. The (statistical) evaporation of light particles, that may occur just before the beginning of the binary decay process of cluster emission studied here, is not included in this paper. Finally, a summary and discussion of our results is added in Sec. 4.

2 THE DYNAMICAL CLUSTER DECAY MODEL

The dynamical cluster-decay model developed here for hot compound nucleus is an adaptation of the preformed cluster model (PCM) of Gupta et al. [24, 25, 26, 27, 28] for ground-state decays, which itself is based on the well-known quantum mechanical

fragmentation theory, the QMFT [29, 30, 31], given for fission and heavy-ion reactions and used later for the prediction of exotic cluster radioactivity [9, 32, 33]. In the preformed cluster model, the decay half-life $T_{\frac{1}{2}}$, or the decay constant λ , is defined as

$$\lambda = \frac{\ln 2}{T_{\frac{1}{2}}} = P_0 \nu_0 P, \quad (1)$$

where P_0 , the preformation probability, refers to the motion in the mass asymmetry coordinate $\eta=(A_1-A_2)/(A_1+A_2)$ and P , the penetrability, to the motion in the relative separation coordinate R . This means that, like in PCM, we treat the distribution of the IMFs as a dynamical collective mass motion of preformed fragments or clusters through the barrier. In principle, the η and R motions are coupled, but, in view of the defining Eq. (1) and our earlier works [29, 30, 34], these are taken to be decoupled here. The ν_0 is the assault frequency, defined below. In terms of the partial waves, the compound nucleus decay or the fragments production cross section

$$\sigma = \frac{\pi}{k^2} \sum_{\ell=0}^{\ell_c} (2\ell + 1) P_0 P; \quad k = \sqrt{\frac{2\mu E_{c.m.}}{\hbar^2}} \quad (2)$$

with $\mu = [A_1 A_2 / (A_1 + A_2)] m = \frac{1}{4} A m (1 - \eta^2)$ as the reduced mass and ℓ_c , the critical (maximum) angular momentum, defined later. m is the nucleon mass. This means that λ in (1) gives the cross section for $\ell = 0$ case, with a normalization constant ν_0 , instead of the π/k^2 in (2). However, in the present calculations, made for $\ell = 0$ (s-wave) case, the normalization constant is obtained empirically from the experimental data.

The preformation probability

$$P_0 = \sqrt{B_{\eta\eta}} | \psi(\eta(A_i)) |^2 (2/A), \quad (3)$$

($i=1$ or 2), where $\psi(\eta)$ are related to $\psi^\nu(\eta)$, $\nu=0,1,2,3\dots$ (see Eq.(12)), the eigen-solutions of stationary Schrödinger equation in η , at fixed R ,

$$\left\{ -\frac{\hbar^2}{2\sqrt{B_{\eta\eta}}} \frac{\partial}{\partial \eta} \frac{1}{\sqrt{B_{\eta\eta}}} \frac{\partial}{\partial \eta} + V_R(\eta) \right\} \psi^\nu(\eta) = E^\nu \psi^\nu(\eta), \quad (4)$$

which is solved at $R=R_a$, the first turning point in the inter-nuclear potential (see Fig. 1). For the ground-state ($T=0$) decay $R_a=C_1+C_2=C_t$, fixed empirically, since this value of R (instead of $R=R_0$, the compound nucleus radius) assimilates to a good extent the effects of both the deformations β_i of the two fragments and the neck formation between them [27]. The C_i are the Süssmann central radii $C_i=R_i-(b/R_i)$, with the radii $R_i=1.28A_i^{1/3}-0.76+0.8A_i^{-1/3}$ fm and surface thickness parameter $b=0.99$ fm. Thus, by raising the first turning point R_a from $R_a=R_0$ to $R_a=C_t$ or, in general, $=C_t+\sum \delta R(\beta_i)$, the deformation effects of the two fragments (and the neck formation between them) are included here in the scattering potential $V(R,T=0)$, within the extended model of Gupta and collaborators for both the light and heavy nuclear systems [27, 35, 36]. The

neck-length parameter $\sum \delta R(\beta_i)$, introduced at the scission configuration, simulates the two-centre nuclear shape parametrization and is equivalent to the lowering of the barrier for the case of deformed fragments [27]. This method of inclusion of fragment deformations in the present calculations is quite similar to what has been achieved in both the saddle-point transition-state model of Sanders [3, 4] and the scission-point Extended Hauser-Feshbach Method of Matsuse and collaborators [5]. The work of Ref. [27] also shows that the alternative of calculating the fragmentation potential $V(\eta)$ and scattering potential $V(R)$ for actual deformations of the nuclei is not practical since the experimental deformation parameters for all the possible fragments (A_1, A_2), required for calculating $V(\eta)$, are generally not available. Note that the deformation effects of nuclei in the present calculations are also included via the Süssmann central radii C_i and that C_t are different for different η -values and hence C_t is $C_t(\eta)$. The temperature effects on radii R_i , and hence on C_i , the neck-length parameter $\delta R(\beta_i)$ and the surface width b are discussed in the following.

For the decay of a hot compound nucleus, we follow the prescription of our earlier work [10] and define the first turning point

$$R_a(T) = C_t(\eta, T) + \Delta R(\eta, T), \quad (5)$$

which means changing R_a to $R_a + \Delta R$ for the hot compound nucleus. Note that C_t and ΔR are also taken temperature-dependent, as defined later. Fig. 1 illustrates the scattering potential and other quantities of interest. Apparently, ΔR depends on the total kinetic energy $TKE(T)$, and the corresponding potential $V(R_a)$ acts like an effective Q-value, $Q_{eff}(T)$. Since, $R_a=C_t(\eta)$ for $T=0$, the $\Delta R(\eta)$ corresponds to the change in TKE at T with respect to its value at $T=0$ and $R_a=C_t$, and hence can be estimated exactly for the temperature effects included in the scattering potential $V(R)$.

We define $Q_{eff}(T)$ in terms of the binding energies of the hot compound system and of the cold ($T=0$) fragments, as

$$\begin{aligned} Q_{eff}(T) &= B(T) - [B_1(T=0) + B_2(T=0)] \\ &= TKE(T) \\ &= V(R_a), \end{aligned} \quad (6)$$

meaning thereby that the decaying hot compound system, which is at temperature T at $R=R_a$, comes out of the barrier and gives in the exit channel two fragments that are cold ($T=0$). These two fragments in the exit channel go to ground state ($T=0$) by emitting some light particle(s) and/or γ -ray(s) of energy (see Fig. 1)

$$\begin{aligned} E_x &= B(T) - B(0) \\ &= Q_{eff}(T) - Q_{out}(T=0) \\ &= TKE(T) - TKE(T=0). \end{aligned} \quad (7)$$

This can be understood by writing from Eq. (7) or (6)

$$Q_{eff}(T) = TKE(T)$$

$$\begin{aligned}
&= Q_{out}(T=0) + E_x \\
&= TKE(T=0) + E_x,
\end{aligned} \tag{8}$$

which means that the fragments are observed in the ground state with $Q_{out}(T=0)$ (or $=TKE(T=0)$) and light particle(s) and/or γ -rays emitted with energy E_x . The remaining excitation energy of the decaying system is then,

$$E_{CN}^* - E_x = |Q_{out}(T)| + TKE(T=0) + TXE(T), \tag{9}$$

where, in the exit-channel the compound nucleus excitation energy E_{CN}^* ($=E_{c.m.} + Q_{in}$, the sum of the entrance-channel centre-of-mass energy $E_{c.m.}$ and the corresponding Q-value, $Q_{in}=-67.59$ MeV for $^{58}\text{Ni}+^{58}\text{Ni}\rightarrow^{116}\text{Ba}$) plus the (positive) Q-value of exit-channel fragments at temperature T , $Q_{out}(T)$, is distributed into the total excitation energy (TXE) and total kinetic energy (TKE) of the two outgoing fragments,

$$E_{CN}^* + Q_{out}(T) = TKE(T) + TXE(T). \tag{10}$$

Eq. (9) again shows that the exit channel fragments are obtained with their TKE in the ground-state, i.e. with $TKE(T=0)$. The excitation energy $TXE(T)$ in (9) is used in the secondary emission of light particles from the primary fragments, which are on the average one α -particle to two-nucleons [15], but are not treated here. Instead, we compare our calculations with the primary pre-secondary-evaporation fragments emission data, if available.

Note that in Eq. (5), ΔR depends on η . In the following, however, based on our earlier works [10, 22] and the works of other authors [4, 5] (discussed later), we use a constant average value $\overline{\Delta R}$, independent of η , which also takes care of the additional $\sum \delta R(\beta_i)$ effects of the deformations of fragments and neck formation between them. The $\overline{\Delta R}$ is the only parameter of the model, though we shall see later that the structure of the calculated (s-wave) mass spectrum is nearly independent of the exact choice of this parameter value. Thus, in our calculations, Eq. (5) is reduced to

$$R_a(T) = C_t(\eta, T) + \overline{\Delta R}(T). \tag{11}$$

Hence, at temperature T , the preformation factor P_0 in Eq. (3) is calculated for $R=R_a(T)$ of Eq. (11), with the temperature effects also included in $\psi(\eta)$ through a Boltzmann-like function

$$|\psi|^2 = \sum_{\nu=0}^{\infty} |\psi^\nu|^2 \exp(-E^\nu/T). \tag{12}$$

The compound nucleus temperature T (in MeV) is given by

$$E_{CN}^* = (A/9)T^2 - T. \tag{13}$$

The penetrability P is the WKB tunnelling probability,

$$P = \exp\left[-\frac{2}{\hbar} \int_{R_a}^{R_b} \{2\mu[V(R) - Q_{eff}]\}^{1/2} dR\right]. \tag{14}$$

This expression is solved analytically [25]. Here R_b is the second turning point. For the penetrability P , Eq.(11) means that

$$V(R_a) = V(C_t(\eta, T) + \overline{\Delta R}(T)) = V(R_b) = Q_{eff}(T) = TKE(T). \quad (15)$$

In Eq.(4), the fragmentation potential $V_R(\eta)$ at any temperature T is calculated within the Strutinsky renormalization procedure, as

$$\begin{aligned} V_R(\eta, T) &= \sum_{i=1}^2 [V_{LDM}(A_i, Z_i, T)] + \sum_{i=1}^2 [\delta U_i] \exp(-\frac{T^2}{T_0^2}) \\ &+ \frac{Z_1 Z_2 e^2}{R(T)} + V_P(T) + V_\ell(T), \end{aligned} \quad (16)$$

where, as already stated in the Introduction, the T -dependent liquid drop energy $V_{LDM}(T)$ is that of Ref. [13], and shell corrections $\delta U(T)$ are considered to vanish exponentially, with $T_0 = 1.5$ MeV. The $V_{LDM}(T)$ has the following form, based on the semi-empirical mass formula of Seeger [37],

$$\begin{aligned} V_{LDM}(A, Z, T) &= \alpha(T)A + \beta(T)A^{\frac{2}{3}} + \left(\gamma(T) - \frac{\eta(T)}{A^{\frac{1}{3}}}\right) \\ &\times \left(\frac{I^2 + 2|I|}{A}\right) + \frac{Z^2}{r_0(T)A^{\frac{1}{3}}}\left(1 - \frac{0.7636}{Z^{\frac{2}{3}}}\right) \\ &- \frac{2.29}{[r_0(T)A^{\frac{1}{3}}]^2} + \delta(T)\frac{f(Z, A)}{A^{\frac{3}{4}}}, \end{aligned} \quad (17)$$

with

$$I = a_a(Z - N), \quad a_a = 1,$$

and, respectively, for even-even, even-odd, and odd-odd nuclei,

$$f(Z, A) = (-1, 0, 1).$$

Seeger [37] fitted the constants from the ground-state ($T=0$) binding energies of some 488 nuclei available at that time (in 1961), and obtained:

$$\alpha(0) = -16.11 \text{ MeV}, \quad \beta(0) = 20.21 \text{ MeV},$$

$$\gamma(0) = 20.65 \text{ MeV}, \quad \eta(0) = 48.00 \text{ MeV},$$

and from Ref. [38], the pairing energy term

$$\delta(0) = 33.0 \text{ MeV}.$$

These constants apparently need to be re-fitted to the large amount of data on ground-state binding energy available now [39], particularly for neutron-rich nuclei. This is partly done in Ref. [22] and is extended here to nuclei upto $Z=56$. The constants

required to be fitted again are the bulk constant $\alpha(0)$, working as an overall scaling factor, and the proton-neutron asymmetry constant a_a , controlling the curvature of the experimental parabola, illustrated in Fig. 2 by the open circles for $Z=49$ nuclei. Note the excellent agreement between the present fits (open circles) and the compilation of experimental data of Ref. [39] (solid circles). The fits are obtained within 1 to 1.5 MeV of the measured binding energies. Table 1 gives as an example the fitted constants for $1 \leq Z \leq 56$ nuclei, which includes the ones in Table 1 of Ref. [22]. The kind of improvement obtained is further illustrated in Fig. 3 for the fragmentation potentials, used in the present calculations (compare the newly fitted binding energies displayed as open circles with the experimental binding energies displayed as solid circles [39]). The two curves are almost identical, particularly for the positions of maxima and minima.

The temperature dependence of the constants in Eq. (17) was obtained numerically in Ref.[13] by using the available experimental information on excited states of 313 nuclei in the mass region $22 \leq A \leq 250$ for determining the partition function $\mathcal{Z}(A,Z,T)$ of each nucleus in a canonical ensemble (see Ref. [13] for further details) and making a least squares fit of the excitation energy $E_{ex}(A, Z, T) = V_{LDM}(A, Z, T) - V_{LDM}(A, Z, 0)$ to the ensemble average $E_{ex}(A, Z, T) = T^2 \frac{\partial}{\partial T} \ln \mathcal{Z}(A, Z, T)$. The $\alpha(T)$, $\beta(T)$, $\gamma(T)$, $\eta(T)$ and $\delta(T)$ thus obtained are given in Figure 1 of Ref. [13] for $T \leq 4\text{MeV}$, extrapolated linearly for higher temperatures. The $\delta(T)$ is constrained to be positive definite at all temperatures, with $\delta(T > 2 \text{ MeV}) = 0$. For the bulk constant $\alpha(T)$, the authors also give the following empirically fitted equation to a Fermi gas model,

$$\alpha(T) = \alpha(0) + \frac{T^2}{15},$$

which is used here in our calculations with the re-fitted $\alpha(0)$. Finally, for the radius constant $r_0(T)$ in (17), the analytical form, taken from Ref. [40], is

$$r_0(T) = 1.07(1 + 0.01T). \quad (18)$$

This means that $R_i (=r_0 A_i^{\frac{1}{3}})$, and in turn C_i , are T-dependent.

The shell effects δU , added to the liquid drop energy in Eq. (16), are obtained empirically by Myers and Swiatecki [41], for spherical shapes, as

$$\delta U = C \left[\frac{F(N) + F(Z)}{(A/2)^{\frac{2}{3}}} - cA^{\frac{1}{3}} \right] \quad (19)$$

with

$$F(X) = \frac{3}{5} \left(\frac{M_i^{\frac{5}{3}} - M_{i-1}^{\frac{5}{3}}}{M_i - M_{i-1}} \right) (X - M_{i-1}) - \frac{3}{5} \left(X^{\frac{5}{3}} - M_{i-1}^{\frac{5}{3}} \right) \quad (20)$$

where $X=N$ or Z , $M_{i-1} < X < M_i$. M_i are the magic numbers 2,8,14 (or 20), 28,50,82,126 and 184 for both neutrons and protons. The constants are $C=5.8$ MeV and $c=0.26$ MeV. We refer to the use of magic numbers 14 or 20 as MS14 or MS20 parametrization.

The V_P in Eq. (16) is the additional attraction due to the nuclear proximity potential [42], also taken to be temperature-dependent, as

$$V_P(R, T) = 4\pi\bar{R}(T)\gamma b(T)\Phi(s, T), \quad (21)$$

where $\bar{R}(T)$ is the inverse of the root mean square radius of the Gaussian curvature and $\Phi(s, T)$ is the universal function, independent of the geometry of the system, given by

$$\Phi(s, T) = \begin{cases} -\frac{1}{2}(s - 2.54)^2 - 0.0852(s - 2.54)^3 & \text{for } s \leq 1.2511 \\ -3.437\exp(-\frac{s}{0.75}) & \text{for } s \geq 1.2511 \end{cases} \quad (22)$$

$$\bar{R}(T) = \frac{C_1(T)C_2(T)}{C_t(T)}. \quad (23)$$

Furthermore, γ is the specific nuclear surface tension given by

$$\gamma = 0.9517 \left[1 - 1.7826 \left(\frac{N - Z}{A} \right)^2 \right] \text{MeV fm}^{-2}. \quad (24)$$

In Eq. (22), $s(T)$ ($=\frac{R-C_t(T)}{b(T)}$) is the overlap distance, in units of b , between the colliding surfaces. The surface width b is [14]

$$b(T) = 0.99(1 + 0.009T^2). \quad (25)$$

Thus, in $C_i = R_i - (b/R_i)$, the T -dependence is via both R_i and b .

The same temperature dependence of $r_0(T)$, given by Eq. (18), is also used for the Coulomb potential $E_c(T) = Z_1Z_2e^2/r_0(T)A^{1/3}$ where the charges Z_i are fixed by minimizing the potential $V_R(\eta, T)$ in the charge asymmetry coordinate $\eta_Z=(Z_1-Z_2)/(Z_1+Z_2)$. The V_ℓ is the centrifugal potential. However, like in Refs. [10, 22], we consider here only the $\ell=0$ case ($V_\ell=0$) since the s-wave is shown to contain the gross information about both the measured fragment emission yields and their total kinetic energies. For a detailed description, however, the angular momentum effects must also be included, which we wish to do in our next publication.

The mass parameters $B_{\eta\eta}(\eta)$, representing the kinetic energy part in Eq. (4), are the smooth classical hydrodynamical masses [43], since we are dealing here with a situation where the shell effects are almost completely washed out. In the classical hydrodynamical model, for touching spheres, we use

$$B_{\eta\eta} = \frac{AmC_t^2(T)}{4} \left(\frac{v_t(T)(1 + \beta(T))}{v_c(T)} - 1 \right) \quad (26)$$

with

$$\beta(T) = \frac{R_c(T)}{4C_t(T)} \left(2 - \frac{R_c(T)}{C_1(T)} - \frac{R_c(T)}{C_2(T)} \right) \quad (27)$$

$$v_c(T) = \pi R_c^2(T)C_t(T), \quad R_c(T) = 0.4C_2(T), \quad (28)$$

and $v_t = v_1 + v_2$, the total conserved volume. Also, $C_2 \ll C_1$ and $R_c (\neq 0)$ is the radius of a cylinder of length C_t , whose existence allows a homogeneous, radial flow of mass between the two fragments. Note that here all radial or radial-dependent quantities are temperature-dependent, with $R_i(T) = r_0(T)A_i^{1/3}$ fm in C_i and C_t . The above expressions are also used for T-independent calculations, but then with $R_i = 1.28A_i^{1/3} - 0.76 + 0.8A_i^{-1/3}$ fm.

In Eq.(1), the assault frequency ν_0 is given simply as

$$\nu_0 = \frac{(2E_2/\mu)^{1/2}}{R_0}, \quad (29)$$

with the kinetic energy of the lighter fragment $E_2 = (A_1/A)Q_{eff}$, where Q_{eff} is shared between the two fragments as inverse of their masses. However, for the calculations of s-wave cross sections, instead of ν_0 , we use an empirically determined normalization constant.

Finally, the temperature-dependent scattering potential $V_\eta(R, T)$, normalized to the exit channel binding energy, is

$$V_\eta(R, T) = \frac{Z_1 Z_2 e^2}{R(T)} + V_P(T), \quad (30)$$

with $R_i(T) = r_0(T)A_i^{1/3}$ fm. This is illustrated in Fig. 1. For T-independent case $R_i = 1.28A_i^{1/3} - 0.76 + 0.8A_i^{-1/3}$ fm. Eq. (30) means that for fixed η , the energies are measured w.r.t. $B_1(T) + B_2(T)$, and the fragments go to ground state ($T \rightarrow 0$) only via the emission of particle(s) or γ -ray(s) of energy E_x .

3 CALCULATIONS

In this section, we present our calculations in such a way that the role of temperature is emphasised in the different terms of the potential. For this purpose, we first look at our calculations for the temperature effects only in liquid drop energy and shell corrections, i.e. for use of $V_{LDM}(T)$ and $\delta U(T)$, but T-independent E_c and V_P . Note that this is already a first improvement over our earlier calculation in [10], where only shell corrections were taken to be T-dependent. Then, as a second and final improvement, we include the T-dependence in all terms of the potential, i.e. we use $V_{LDM}(T)$, $\delta U(T)$, $E_c(T)$ and $V_P(T)$. The resulting fragmentation potentials for ^{116}Ba are given in the following two subsections, respectively, for each case. Only s-wave ($\ell = 0$) solutions are studied here in the following.

3.1 Temperature-dependence only in liquid drop energy and shell correction

Figure 4 gives our calculated fragmentation potentials $V(\eta)$ for cold ($T=0$) as well as hot $^{116}\text{Ba}^*$ nucleus at various T-values referring to compound nucleus excitation energies

E_{CN}^* of the experiments of Refs. [2, 17]. Comparing with our earlier calculation [10], here the liquid drop potential V_{LDM} is also T-dependent. The R_a -value for each T-value is chosen as follows: At T=0, $R_a=C_t$, as is already discussed above. For hot compound systems, we fix $R_a=C_t + \overline{\Delta R}$ with $\overline{\Delta R} = 0.226, 0.252, 0.281, \text{ and } 0.466$ fm (chosen arbitrarily), respectively, for T=2.91, 3.06, 3.20, and 4.42 MeV, which correspond to the four experimental values of $E_{c.m.}=174, 185.5, 197, \text{ and } 315$ MeV of Refs. [17] and [2]. We notice that, as far as the fine structure is concerned, the calculations are nearly independent of the exact choice of $\overline{\Delta R}$ -value, which is explicitly illustrated in Fig. 5 for T=4.42 MeV. This observation has already been made in our earlier studies on QMFT [28, 31]. As a consequence, the same is true for the calculated yields shown below in Figs. 8 and 9. Thus, for a given $E_{c.m.}$, $\overline{\Delta R}$ is fixed for all the fragments; on the other hand $\overline{\Delta R}$ was fitted for each fragment separately in our earlier work [10], as well as in the statistical model calculations of other authors [4, 5]. Note, the $\overline{\Delta R}$ in our model is the same as the neck length parameter d in Refs. [4, 5].

We notice in Fig. 4 that, due to the T-dependence of V_{LDM} , the fragmentation potentials show large differences as compared to our earlier calculations in Ref. [10]. First of all, the α -like structure, present at all T values in our earlier calculations, including the extreme case of T=4.42 MeV where $\delta U(T)$ is reduced almost to zero, is now washed out, even at the lowest temperature. The potential energy surfaces are now smooth for the heavier fragments at all T values, and new non- α fragments appear in the lighter mass region. In other words, with increased T, not only the shell structure effects go to zero but also the preference for α -like structure, due to the Wigner term, vanishes. Also, the light particle ($A \leq 3$) structure is found to change with T. Thus, with T added, the significant structure in $V(\eta)$ seems to remain only for a small window of light fragments having masses less than ~ 20 , and we refer to it as the "IMF window" in the following.

Figure 6 shows the preformation factor P_0 for the IMF window only, calculated for the four chosen experimental temperatures. We notice that the formation yields increase as T increases and that some of the fragments are strongly preformed compared to their neighbours. Also, the yields for fragments with masses $A_2 > 16$ are very small, with ^{12}C being better preformed at higher energies. The lighter particles ($A \leq 3$), other than the statistically evaporated ones (not considered here), are also equally strongly preformed and a neutron (n) at lower energies changes to a proton (^1H) at higher energies. However, the final decay constant (equivalently, the IMF s-wave production cross section) is a combined effect of P_0 and P , the ν_0 being almost constant. The result of this calculation is presented in Fig. 7 for all the strongly preformed and observed IMFs ($Z < 9, A \leq 18$) at the four experimental energies. Some of the light particle emissions (n and ^2H) are not shown here since their Q_{eff} values are negative (or nearly zero) for all the T and R_a values considered here (the dependence of the decay constant λ on R_a is already studied in our earlier work [10]; see also Fig. 9 below). For ^1H , Q_{eff} is positive only for the two higher energies corresponding to T=3.20 and 4.42 MeV.

The role of the penetrability P is evident in Fig. 7, since some of the strongly

performed fragments, like ${}^4\text{He}$ and ${}^6\text{Li}$, are now shown as less favoured decays (smaller decay constants). ${}^4\text{He}$, which has the largest preformation factor and decay constant for the ground-state decay (see Figs. 3 and 4 in Ref. [10]), lies here lowest for the hot ${}^{116}\text{Ba}^*$. On the other hand, the other two light particle (${}^1\text{H}$ and ${}^3\text{He}$) decays become the most probable ones at all T values here, and are kind of competing with the so-called statistically evaporated particles. Also, the non- α like decays, like ${}^{10}\text{B}$ and ${}^{14}\text{N}$, with relatively low P_0 's, are now the most predominant ones. In other words, with the T-dependence of V_{LDM} included, the exclusive preference for α -like IMFs seems lost, the decay rates for non- α like decays are higher, and the light particle production rates are the highest. However, the ${}^{12}\text{C}$ decay is still striking since it is the best α -nucleus decay even now, particularly at lower energies (inspite of the lower preformation factor P_0 at these energies). At higher energies, the lighter α -like fragment ${}^8\text{Be}$ competes with it, though we know that ${}^8\text{Be}$ is unbound in the ground state. Note that the charge number Z changes with T for some fragments (here for the mass 17 fragment) and hence at higher T's the measurements of charge distributions become equally important [1, 16]. The sudden increase in the production cross section (λ -value) for ${}^{17}\text{F}$ at $T \geq 3.2$ MeV is due to its enhanced penetrability P, the Q-value effect. (The same effect is observed later in Fig. 13 for T-dependence in all terms of the potential, but at higher temperature $T=4.42$ MeV only).

Fig. 8, upper panel, shows the IMF production cross sections σ for $Z_2 \leq 9$, measured as compound nucleus decays at $E_{c.m.}=315$ MeV [2], compared with our calculated s-wave production cross sections i.e. λ -values for $\overline{\Delta R}=0.466$ *normalized* to the experimental data for $Z_2=6$ fragment decay. The calculated yields are for the energetically favoured, most probable fragments in both the mass and charge numbers (see Figs. 4 and 6) and hence the yields for the same Z_2 but different masses are summed up. For example, the fragments contributing to the $Z_2=6$ fragment yield are the ${}^{11}\text{C}$, ${}^{12}\text{C}$, and ${}^{13}\text{C}$ fragments, and the same to the $Z_2=7$ fragment yield are the ${}^{14}\text{N}$ and ${}^{15}\text{N}$ fragments, etc. For $Z_2=4$, however, we should be cautious in making this comparison between the experiment and calculation since ${}^8\text{Be}$, being unbound as a ground state, may not be measured, but we have included it in our summed yields for $Z_2=4$ (the other component is ${}^9\text{Be}$, with a rather small yield $\sim 10^{-4}$). The lower panel shows the same for another normalization of our calculations to the $Z_2=7$ fragment data. Furthermore, Fig. 9 presents the same comparison (only for normalization to the $Z_2=6$ fragment data) for another two $\overline{\Delta R}$ values. Apparently, the calculations compare reasonably well with experiment and are almost independent of the (empirical) normalization constant as well as the exact choice of $\overline{\Delta R}$ value. For the heavier fragments ($Z_2 \geq 8$), the calculated cross sections are rather small firstly because we are considering here the contribution of only $\ell = 0$ term and secondly because the temperature effects are included only in V_{LDM} and δU . Also, in experiments [2, 15] the contributions from other sources such as the peripheral collisions like projectile splitting or deep-inelastic-like mechanism are difficult to be separated out for the heavy fragments. Thus, in view of the fact that we are dealing here with only the $\ell = 0$ case and that the temperature effects are not fully included in the potential, the comparisons between the theory and experiments

in Figs. 8 and 9 could be considered rather satisfactory.

A comparison of our calculations with the experimental data at the other three lower energies [17] is shown in Fig. 10 for only the four heavy residues ^{99}Cd , ^{100}In , ^{101}Sn and ^{102}In that have been actually measured at each of these three energies, as reported in Ref. [17] (see Fig. 2 and Table 1 of [17]). In this case, the calculations have been normalized arbitrarily to the $A_1=102$ fragment. Some calculated fragments show a change of fragment charge number since we have considered here only the energetically favoured, most probable fragment in both mass and charge numbers which could be different from the one actually measured. The comparison shows that the predicted yields are in reasonable agreement with the experimental data.

3.2 Temperature-dependence of the full potential

Figure 11 gives the calculated fragmentation potentials $V(\eta, T)$ for T-dependence added in all the terms of the potential (Eq. (16), for $\ell = 0$). The T and $\overline{\Delta R}$ values are the same as in Fig. 4 for no T-effects in E_c and V_P . (The graph for T=0 is again shown here for comparisons). We notice that there is hardly any sizeable effect due to the additional T-dependences in E_c and V_P , when Fig. 11 is compared with Fig. 4, at least for the structure and positions of minima, especially at lower T-values. At higher T-values, there are some very small changes, particularly for very light fragments ($A_2 \leq 2$). It is known [44] that V_P does not contribute towards the structure and positions of minima in the fragmentation potential $V(\eta)$ and that E_c is a smoothly increasing function of A_2 . However, the mass parameters $B_{\eta\eta}$, though smooth, are now T-dependent, and this behaviour seems to enhance the formation probability P_0 , presented in Fig. 12. The enhancement is by about one order of magnitude (compare Fig. 12 with Fig. 6 without T-dependence in E_c , V_P , and $B_{\eta\eta}$). As a consequence, we note that in the formation yield of ^{12}C , relative to its neighbouring fragments, the small peaked structure present in Fig. 6 is now absent in Fig. 12.

Figure 13 presents the result of our calculation for the decay constant λ (equivalently, the s-wave production cross section) as a function of compound nucleus temperature corresponding to four energies (174, 185.5, 197, and 315 MeV) of the two selected experimental data sets of Refs. [2, 17]. We notice important differences with respect to the case of no temperature in E_c and V_P (compare Fig. 13 with Fig. 7). Here, for light particles, instead of only ^1H and ^4He at higher temperatures, we get ^2H , ^3H and ^4He at all the temperatures which is favoured by the experimental data (for the neutron, the Q_{eff} is still negative). Note that here these light fragments are not the statistically treated prompt particles, though the calculated yields are shown to be large (calculations made so far are only for the $\ell = 0$ case). Interesting enough, ^{12}C decay is still the most favoured α -nucleus decay, though other non- α fragments are shown to compete. Also, some fragments having smaller cross sections at lower energies are shown to have enhanced cross sections at the higher energy.

Finally, a comparison of our calculated s-wave cross sections with the measured cross sections is made in Figs. 14 and 15. Fig. 14 shows this comparison for the $E_{c.m.}=315$

MeV data [2] with our calculated decay constants (s-wave cross sections) normalized to $Z_2=6$ fragment data. Similarly, Fig. 15 gives a comparison of our calculations with the measured cross sections for the three lower energies of Ref. [17]. Here the data are obtained for only the heavy fragments and we have normalized our calculations to the mass 102 fragment. The comparisons between the calculations and data are rather good at all energies, and better than for the earlier case displayed in Figs. 8, 9 and 10. The improvement demonstrates the need of including temperature dependence in all the terms of the potential.

4 Summary and discussion

Summarizing, first the use of T-dependent V_{LDM} is studied for the cluster decay process proposed for the IMFs emission [10] induced in heavy-ion collisions at low bombarding energies ($E_{c.m.} < 15$ MeV/A). The model is extended and applied to $^{58}\text{Ni}+^{58}\text{Ni}\rightarrow^{116}\text{Ba}^*$ at various centre-of-mass energies from 174 to 315 MeV. Interesting and important enough, with the use of a T-dependent V_{LDM} (for $\ell=0$ case only), the explicit preference for α -like IMFs (or clusters) is lost, though the ^{12}C (or ^{104}Sn) decay (first expected from the ground state decay of ^{116}Ba [18, 19]) is still found to be the most preferred α -like fragment. Also, the non- α IMFs and some light particles with $Z<2$ are shown to be produced with larger yields, without the inclusion of any statistical evaporation process. With T-dependence included in all the terms of the potential, the production yields are enhanced and comparisons with data are improved. Further improvements are expected with the inclusion of contributions from all ℓ -waves, which is being worked out.

Also, the TKEs are measurable quantities, but the same are available for the $^{58}\text{Ni}+^{58}\text{Ni}$ reaction only for $E_{c.m.}=315$ MeV [2] and at only one angle and four charges (without the mass identification of IMFs). In our model, as already defined above and in Fig. 1, the angle-integrated total kinetic energies are given by $\text{TKE}=V(R_a)=V(C_t+\Delta R)=Q_{eff}$. Since the calculated production yields are almost independent of the (arbitrarily) chosen average $\overline{\Delta R}$ values, only the relative variation and not the absolute magnitude of TKEs could be obtained at present in this model. Furthermore, the angular momentum contribution (not included as yet) is a must for TKEs calculations. Such type of calculations have already been performed [22] for the lighter system $^{32}\text{S}+^{24}\text{Mg}\rightarrow^{56}\text{Ni}$ where the angle integrated TKEs data were available [3]. It will be interesting to apply similar considerations to $^{116}\text{Ba}^*$ when similar data on TKEs become available. Also, it would be of interest if the statistical fission model, as introduced in the GEMINI code [1] could also be applied to the $^{58}\text{Ni}+^{58}\text{Ni}$ reaction and its predictions compared with the present cluster decay model results as well as to the pure Hauser-Feshbach BUSCO results. Furthermore, a similar comparison using the alternate picture as generalized liquid-drop model [12] or the so-called unified fission models for cluster decay studies [9] is called for since these models do not introduce any preformation factor.

5 ACKNOWLEDGMENTS

This work is supported in parts by the Council of Scientific and Industrial Research (CSIR) and the Department of Science and Technology (DST), New Delhi, India. The IN2P3/Université Louis Pasteur and IReS Strasbourg, France and the VW-Stiftung, Germany are also acknowledged for financial supports.

References

- [1] R.J. Charity, M.A. McMahan, G.J. Wozniak, R.J. McDonald, L.G. Moretto, D.G. Sarantites, L.G. Sobotka, G. Guarino, A. Pantaleo, F. Fiore, A. Gobbi, and K.D. Hildenbrand, Nucl. Phys. A **483**, 43 (1988).
- [2] J. Gomez del Campo, R.L. Auble, J.R. Beene, M.L. Halbert, H.J. Kim, A. D'Onofrio, and J.L. Charvet, Phys. Rev. C **43**, 2689 (1991).
- [3] S.J. Sanders, D.G. Kovar, B.B. Back, C. Beck, D.J. Henderson, R.V.F. Janssens, T.F. Wang, and B.D. Wilkins, Phys. Rev. C **40**, 2091 (1989).
- [4] S.J. Sanders, Phys. Rev. C **44**, 2676 (1991).
- [5] T. Matsuse, C. Beck, R. Nouicer, and D. Mahboub, Phys. Rev. C **55**, 1380 (1997).
- [6] L.G. Moretto, Nucl. Phys. A **247**, 211 (1975).
- [7] R. Vandenbosch and J.R. Huizenga, *Nuclear Fission*, Academic Press, New York 1973.
- [8] S.J. Sanders, A. Szanto de Toledo, and C. Beck, Phys. Rep. **311**, 487 (1999), and references therein.
- [9] R.K. Gupta and W. Greiner, Int. J. Mod. Phys. E **3**, 335 (1994), Supp.
- [10] R.K. Gupta, M. Balasubramaniam, C. Mazzocchi, M. La Commara, and W. Scheid, Phys. Rev. C **65**, 024601 (2002).
- [11] M. Beckerman, J. Ball, H. Enge, M. Salomaa, A. Sperduto, S. Gazes, A. DiRienzo, and J.D. Molitoris, Phys. Rev. C **23**, 1581 (1981).
- [12] G. Royer and R. Moustabchir, Nucl. Phys. A **683**, 182 (2001).
- [13] N.J. Davidson, S.S. Hsiao, J. Markram, H.G. Miller, and Y. Tzeng, Nucl. Phys. A **570**, 61c (1994).

- [14] G. Royer and J. Mignen, *J. Phys. G: Nucl. Phys.* **18**, 1781 (1992).
- [15] J. Gomez del Campo, J.L. Charvet, A. D'Onofrio, R.L. Auble, J.R. Beene, M.L. Halbert, and H.J. Kim, *Phys. Rev. Lett.* **61**, 290 (1988).
- [16] J. Gomez del Campo, C. Baktash, H.-Q. Jin, D. Rudolph, A. D'Onofrio, F. Terrasi, G. de Angelis, M. De Poli, C. Fahlander, A. Gadea, D.R. Napoli, Q. Pan, P. Spolaore, L. De Acuna, D. Bazzacco, S. Lunardi, P.Pavan, C. Rossi-Alvarez, A. Buscemi, R. Zanon, A. De Rosa, L. Campajola, M. La Commara, G. Inglima, V. Roca, M. Romano, M. Sandoli, M. Romoli, A. Ordine, and D. Pierroutsakou, *Phys. Rev. C* **57**, R457 (1998).
- [17] M. La Commara, J. Gomez del Campo, A. D'Onofrio, A. Gadea, M. Glogowski, P. Jarillo-Herrero, N. Belcari, R. Borcea, G. de Angelis, C. Fahlander, M. Gorska, H. Grawe, M. Hellström, R. Kirchner, M. Rejmund, V. Roca, E. Roeckl, M. Romano, K. Rykaczewski, K. Schmidt, and F. Terrasi, *Nucl. Phys. A* **669**, 43 (2000).
- [18] R.K. Gupta, S. Singh, R.K. Puri, and W. Scheid, *Phys. Rev. C* **47**, 561 (1993);
S. Kumar and R.K. Gupta, *Phys. Rev. C* **49**, 1922 (1994);
S. Kumar, D. Bir, and R.K. Gupta, *Phys. Rev. C* **51**, 1762 (1995).
- [19] D.N. Poenaru, W. Greiner, and E. Hourani, *Phys. Rev. C* **51**, 594 (1995);
D.N. Poenaru, W. Greiner, and R. Gherghescu, *Phys. Rev. C* **47**, 2030 (1993).
- [20] Yu.Ts. Oganessian, Yu. A. Lazarev, V.L. Mikheev, Yu.A. Muzychka, I.V. Shirokovsky, S.P. Tretyakova, and V.K. Utyonkov, *Z. Phy. A* **349**, 341 (1994).
- [21] A. Guglielmetti, B. Blank, R. Bonetti, Z. James, H. Keller, R. Kirchner, O. Klepper, A. Piechaczek, A. Plochocki, G. Poli, P.B. Price, E. Roeckl, K. Schmidt, J. Szerypo, and A.J. Westphal, *Nucl. Phys. A* **583**, 867 (1995).
- [22] R.K. Gupta, R. Kumar, N.K. Dhiman, M. Balasubramaniam, W. Scheid, and C. Beck, *Phys. Rev. C* (2003) in press; Preprint available at: <http://arXiv.org/nucl-th/0305033>
- [23] G. Royer, C. Bonilla, and R.A. Gherghescu, *Phys. Rev. C* **67**, 034315 (2003).
- [24] R.K. Gupta, in *Proceedings of the 5th International Conference on Nuclear Reaction Mechanisms*, Varenna, 1988, edited by E. Gadioli (Ricerca Scientifica ed Educazione Permanente, Milano, 1988), p.416.
- [25] S.S. Malik and R.K. Gupta, *Phys. Rev. C* **39**, 1992 (1989).
- [26] R.K. Gupta, W. Scheid, and W. Greiner, *J. Phys. G: Nucl. Part. Phys.* **17**, 1731 (1991).

- [27] S. Kumar and R.K. Gupta, Phys. Rev. C **55**, 218 (1997).
- [28] R.K. Gupta, in *Heavy Elements and Related New Phenomena*, edited by W. Greiner and R.K. Gupta (World Scientific, Singapore, 1999), Vol. II, p. 730.
- [29] J. Maruhn and W. Greiner, Phys. Rev. Lett. **32**, 548 (1974).
- [30] R.K. Gupta, W. Scheid, and W. Greiner, Phys. Rev. Lett. **35**, 353 (1975).
- [31] R.K. Gupta and W. Greiner, in *Heavy Elements and Related New Phenomena*, Ref. [28], Vol. I, pp. 397, 536.
- [32] A. Săndulescu, D.N. Poenaru, and W. Greiner, Sovt. J. Part. Nucl. **11**, 528 (1980).
- [33] H.J. Rose and G.A. Jones, Nature **307**, 245 (1984).
- [34] D.R. Saroha and R.K. Gupta, J. Phys. G: Nucl. Phys. **12**, 1265 (1986).
- [35] H.S. Khosla, S.S. Malik, and R.K. Gupta, Nucl. Phys. A **513**, 115 (1990).
- [36] R.K. Gupta, S. Kumar, and W. Scheid, Int. J. Mod. Phys. E **6**, 259 (1997).
- [37] P.A. Seeger, Nucl. Phys. **25**, 1 (1961).
- [38] S. DeBenedetti, *Nuclear Interactions* (John Wiley and Sons, 1964).
- [39] G. Audi and A.H. Wapstra, Nucl. Phys. A **595**, 4 (1995).
- [40] M. Brack and P. Quentin, Phys. Lett. B **52**, 159 (1974).
- [41] W. Myers and W.J. Swiatecki, Nucl. Phys. **81**, 1 (1966).
- [42] J. Blocki, J. Randrup, W.J. Swiatecki, and C.F. Tsang, Ann. Phys. (N.Y.) **105**, 427 (1977).
- [43] H. Kröger and W. Scheid, J. Phys. G **6**, L85 (1980).
- [44] D.R. Saroha, N. Malhotra, and R.K. Gupta, J. Phys. G: Nucl. Phys. **11**, L27 (1985).

FIGURE CAPTIONS

- Fig. 1. The s-wave scattering potential, illustrated for $^{116}\text{Ba}^* \rightarrow ^{12}\text{C} + ^{104}\text{Sn}$, showing the effect of temperature for its inclusion in all terms of the potential (solid line), i.e. $V(R,T) = E_c(T) + V_P(T)$, with the binding energy $B(T) = V_{LDM}(T) + \delta U(T)$. The decay path is shown to begin at R_a for the $T \neq 0$ case, along with other quantities that are discussed in the text.
- Fig. 2. The mass excess ΔM ($= M_A - A = NM_n + ZM_p + B(Z,N) - A$ in MeV) as a function of neutron number N for $Z=49$ nuclei, calculated by using the 1995 experimental data (solid circles) [39], with newly fitted constants (open circles) and with the 1961 Seeger's constants [37] (open squares).
- Fig. 3. The fragmentation potential for ^{116}Ba at $T=0$, using the experimental binding energies (solid circles) [39] and the empirical binding energies (open circles) with the new constants given in Table 1.
- Fig. 4. The fragmentation potential $V(\eta, R, T)$ for the hot $^{116}\text{Ba}^*$ nucleus, calculated at the ground-state ($T=0$, $R_a = C_t$) and at the various nuclear temperatures T , which correspond to the bombarding energies of the measurements of Refs. [2, 17], and at the indicated R_a -values. The T -dependence is included only in V_{LDM} and δU , i.e. $V(\eta, R, T) = V_{LDM}(T) + \delta U(T) + E_c + V_P$. The thin vertical lines are drawn to mark the exclusive α -like structure present in $T=0$ case only.
- Fig. 5. Same as for Fig. 4, but for only $T=4.42$ MeV and at different $\overline{\Delta R}$ values.
- Fig. 6. The IMFs preformation probability P_0 for the hot $^{116}\text{Ba}^*$ nucleus, calculated for the four experimental T -values corresponding to $E_{c.m.} = 174, 185.5, 197,$ and 315 MeV or equivalently $T = 2.91, 3.06, 3.20$ and 4.42 MeV, respectively, using the fragmentation potentials displayed in Fig. 4.
- Fig. 7. The cluster decay constant $\lambda(\text{s}^{-1})$ as a function of nuclear temperature T for emissions of the IMFs and light particles from the hot $^{116}\text{Ba}^*$ nucleus, calculated at the four experimental T and R_a values used in Fig. 4 that gives the relevant fragmentation potentials. The dashed line shows the change of charge number of the cluster. As for the experimental data of Refs. [2, 15], only the fragments with $Z \leq 9$ are found to be of a compound nucleus origin.
- Fig. 8. The calculated (s-wave) and measured cross sections $\sigma(\text{mb})$ for all the IMFs produced in decay of $^{116}\text{Ba}^*$ at $E_{c.m.} = 315$ MeV. The experimental data are taken from the Fig. 6 of Ref. [2]. Since in experiments [2] only the charges of fragments are measured, in calculations we have summed up the yields for most probable fragments with the same charge but different masses. The calculations are made for $\overline{\Delta R} = 0.466$ fm and are normalized to experimental data of $Z_2 = 6$ fragment (upper panel) and $Z_2 = 7$ fragment (lower panel).

- Fig. 9. Same as for Fig. 8 (upper panel), but for $\overline{\Delta R}=0.578$ fm (upper panel) and 0.8 fm (lower panel).
- Fig. 10. Same as for Fig. 8, but for $E_{c.m.}=174, 185.5$ and 197 MeV [17] and heavy fragments, and for normalization with respect to $A_1=102$ mass fragment. The experimental data are from Table 1 or Fig. 2 of Ref. [17]. Note that the calculated and measured Z -values of some fragments are different since in calculations we have considered only the energetically favoured fragment with most probable charge and mass.
- Fig. 11. Same as for Fig. 4, but for the T -dependence included in all terms of the potential, i.e. $V(\eta,R,T)=V_{LDM}(T)+\delta U(T)+E_c(T)+V_P(T)$. Here the potential for only the light fragments is shown, since it is symmetrical with respect to $A_2=58$ (or $\eta=0$).
- Fig. 12. Same as for Fig. 6, but for the potentials given in Fig. 11, i.e. for T -dependence included in all terms of the potential.
- Fig. 13. Same as for Fig. 7, but for the potentials given in Fig. 11, i.e. for T -dependence included in all terms of the potential. The mass $A_2=1$ fragment (n, in this case) is not shown because Q_{eff} is negative for the chosen parameters of the calculations.
- Fig. 14. Same as for Fig. 8 (upper panel), but for the potentials given in Fig. 11, i.e. for T -dependence included in all terms of the potential.
- Fig. 15. Same as for Fig. 10, but for the potentials given in Fig. 11, i.e. for T -dependence included in all terms of the potential.

Table 1: Re-fitted bulk and asymmetry constants of Seeger's liquid drop energy for $1 \leq Z \leq 56$.

Z	N	$\alpha(0)$	a_a	Z	N	$\alpha(0)$	a_a
1	2	-15.85	0.10	6	4	-15.70	0.10
	3	-16.95	0.12		5,7	-16.50	0.10
	4	-13.00	0.05		6	-16.65	0.10
	5	-13.70	0.12		8	-15.90	0.10
2	1	-15.50	0.10		9	-15.70	0.10
	2	-16.00	0.10		10	-15.10	0.10
	3	-16.80	0.30		11	-14.80	0.10
	4,5	-14.20	0.30		12,13,15,16	-15.00	0.80
	6	-13.50	0.10		14	-14.85	0.80
	7,8	-13.00	0.10	7	3	-14.30	0.20
3	1,2,4,5	-16.60	0.10		4	-15.20	0.50
	3	-16.98	0.98		5	-16.20	0.80
	6	-13.80	0.98		6	-16.55	0.80
	7	-14.30	0.40		7	-16.80	0.80
	8,9	-13.20	0.10		8	-16.30	0.80
4	1	-13.00	0.01		9	-16.20	0.80
	2	-14.50	0.10		10,11	-15.90	0.94
	3	-16.20	0.80		12	-15.75	0.94
	4	-16.98	0.98		13	-15.80	0.94
	5	-16.70	0.60		14	-15.65	0.94
	6	-15.50	0.80		15	-15.90	0.94
	7	-15.30	0.50		16	-16.00	0.94
	8	-14.30	0.10		17	-16.10	0.93
	9	-14.00	0.10	8	4	-14.00	0.94
	10	-13.30	0.01		5	-15.25	0.94
5	2	-14.60	0.10		6	-15.90	0.94
	3	-16.50	0.10		7	-16.35	0.94
	4	-16.60	0.60		8	-16.20	0.94
	5	-16.99	0.10		9	-16.18	0.94
	6	-16.60	0.60		10	-15.95	0.94
	7	-16.30	0.10		11	-15.93	0.94
	8	-15.35	0.10		12,14	-15.85	0.94
	9	-15.10	0.10		13	-15.90	0.94
	10	-14.45	0.10		15	-16.10	0.94
	11	-14.10	0.10		16	-16.15	0.90
	12	-13.45	0.10		17	-16.30	0.92
	13	-13.10	0.10		18	-16.11	0.92
	14	-13.00	0.40	9	5	-15.25	0.90
6	2	-13.00	0.10		6	-15.90	0.90
	3	-13.85	0.80		7	-16.28	0.90

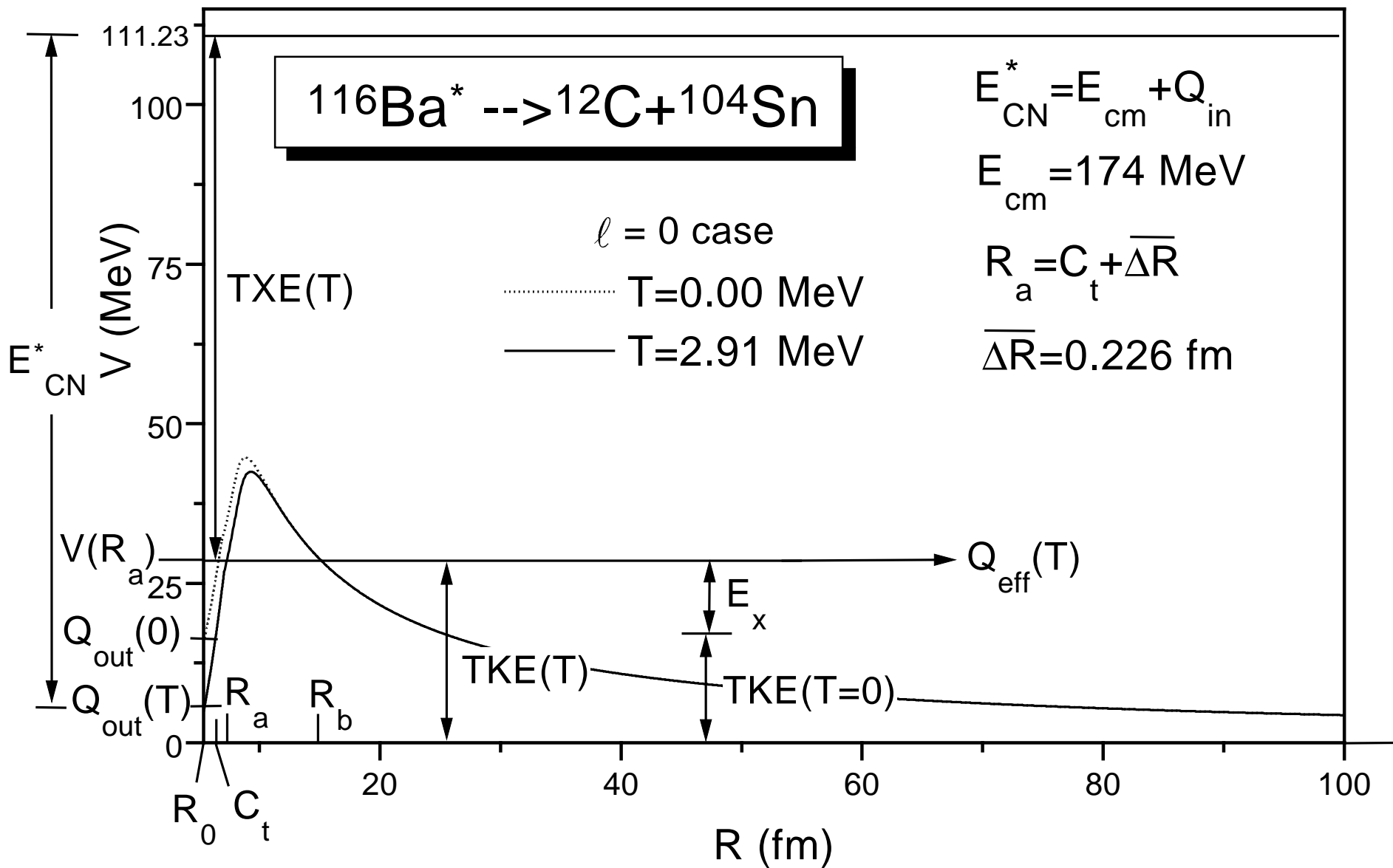
Table 1: Continued.....

Z	N	$\alpha(0)$	a_a	Z	N	$\alpha(0)$	a_a
9	9	-16.30	0.90	21	15-23,31-38	-16.42	0.77
	10	-16.15	0.90		24-30	-16.38	0.78
	8,11,17,19,20	-16.20	0.90	22	16-39	-16.42	0.77
	12	-16.01	0.90	23	17-40	-16.42	0.77
	13	-16.05	0.90	24	18-25	-16.45	0.77
	14	-15.95	0.90		26-41	-16.42	0.77
	15,16,18	-16.11	0.90	25	19-26	-16.46	0.77
10	6	-15.25	0.50		27-42	-16.42	0.77
	7	-15.70	0.50	26	19-43	-16.46	0.77
	8	-15.90	0.90	27	21-28	-16.48	0.77
	13	-15.95	0.50		29-45	-16.46	0.77
	14	-15.70	0.50	28	22-48	-16.48	0.77
	9-12,15-22	-16.16	0.88	29	23-35,49-57	-16.50	0.76
11	7	-15.55	0.50		36-48	-16.48	0.77
	8	-15.80	0.50	30	24-36	-16.50	0.76
	14	-15.95	0.50		37-52	-16.48	0.70
	9-13,15-24	-16.20	0.86	31	25-53	-16.50	0.75
12	8-10	-16.11	0.90	32	26-34	-16.57	0.75
	11-25	-16.20	0.86		35-40,53,54	-16.52	0.75
13	8-10	-16.11	0.90		41-52	-16.50	0.75
	11-26	-16.22	0.84	33	27-36	-16.57	0.75
14	8-12	-16.11	0.90		37-56	-16.52	0.75
	13-20,27,28	-16.28	0.84	34	31-38	-16.57	0.75
	21-26	-16.22	0.84		39-41,53-58	-16.54	0.75
15	9-13,20-31	-16.30	0.82		42-52	-16.52	0.75
	14-19	-16.36	0.78	35	32-41,53-59	-16.56	0.75
16	10-14,21-28	-16.30	0.82		42-52	-16.54	0.75
	15-20	-16.40	0.78	36	33-41	-16.60	0.75
	29-33	-16.32	0.80		42-61	-16.56	0.75
17	11-14,20,21,29-34	-16.36	0.78	37	34-41,59-65	-16.63	0.75
	15-19	-16.45	0.78		42-58	-16.58	0.75
	22-28	-16.32	0.82	38	35-42	-16.63	0.75
18	12-14,21,22,31-35	-16.36	0.78		43-66	-16.59	0.75
	15-20	-16.45	0.78	39	38-43,59-67	-16.63	0.75
	23-30	-16.32	0.78		44-58	-16.61	0.75
19	13,14,22,23,30-36	-16.38	0.78	40	39-42	-16.67	0.75
	15-21	-16.44	0.78		43-68	-16.63	0.75
	24-29	-16.36	0.80	41	40-44	-16.66	0.75
20	14,15,22-37	-16.38	0.78		45-69	-16.63	0.75
	16-21	-16.48	0.78	42	41-45,65-71	-16.68	0.75

Table 1: Continued.....

Z	N	$\alpha(0)$	a_a	Z	N	$\alpha(0)$	a_a
42	46-64	-16.64	0.75	50	58-63	-16.72	0.74
43	42-47,67-72	-16.68	0.75		64-74	-16.69	0.735
	48-66	-16.64	0.75		75-87	-16.67	0.72
44	43-46,69-74	-16.70	0.75	51	52-61	-16.75	0.75
	47-49	-16.68	0.75		62-67,83-88	-16.70	0.72
	50-68	-16.66	0.75		68-82	-16.67	0.72
45	44-49,69-74	-16.70	0.75	52	54-58,85-89	-16.79	0.74
	50-68	-16.67	0.75		59-64,77-84	-16.75	0.74
46	45-49	-16.72	0.75		65-76	-16.73	0.74
	50-53,69-73	-16.70	0.75	53	55-59,83-91	-16.79	0.74
	54-68	-16.68	0.75		60-82	-16.75	0.74
47	47-53,77-80	-16.72	0.74	54	56-59	-16.83	0.74
	54-57	-16.70	0.75		60-63,83-93	-16.79	0.74
	58-76	-16.68	0.74		64-82	-16.77	0.74
48	48-52	-16.75	0.74	55	57-62	-16.83	0.75
	53-55,77-82	-16.72	0.74		63-67,81-84	-16.79	0.74
	56-76	-16.69	0.74		68-80	-16.77	0.74
49	49-53,75-76	-16.75	0.75		85-96	-16.77	0.725
	54-59	-16.72	0.74	56	58-61	-16.85	0.74
	60-74	-16.69	0.74		62,63,89-97	-16.84	0.74
	77-85	-16.67	0.72		64-76	-16.82	0.76
50	50-57	-16.76	0.75		77-88	-16.77	0.725

Fig. 1 Balasubramaniam, Kumar, Gupta, Beck and Scheid, 'Emission of intermediate mass fragments from hot ^{116}Ba'



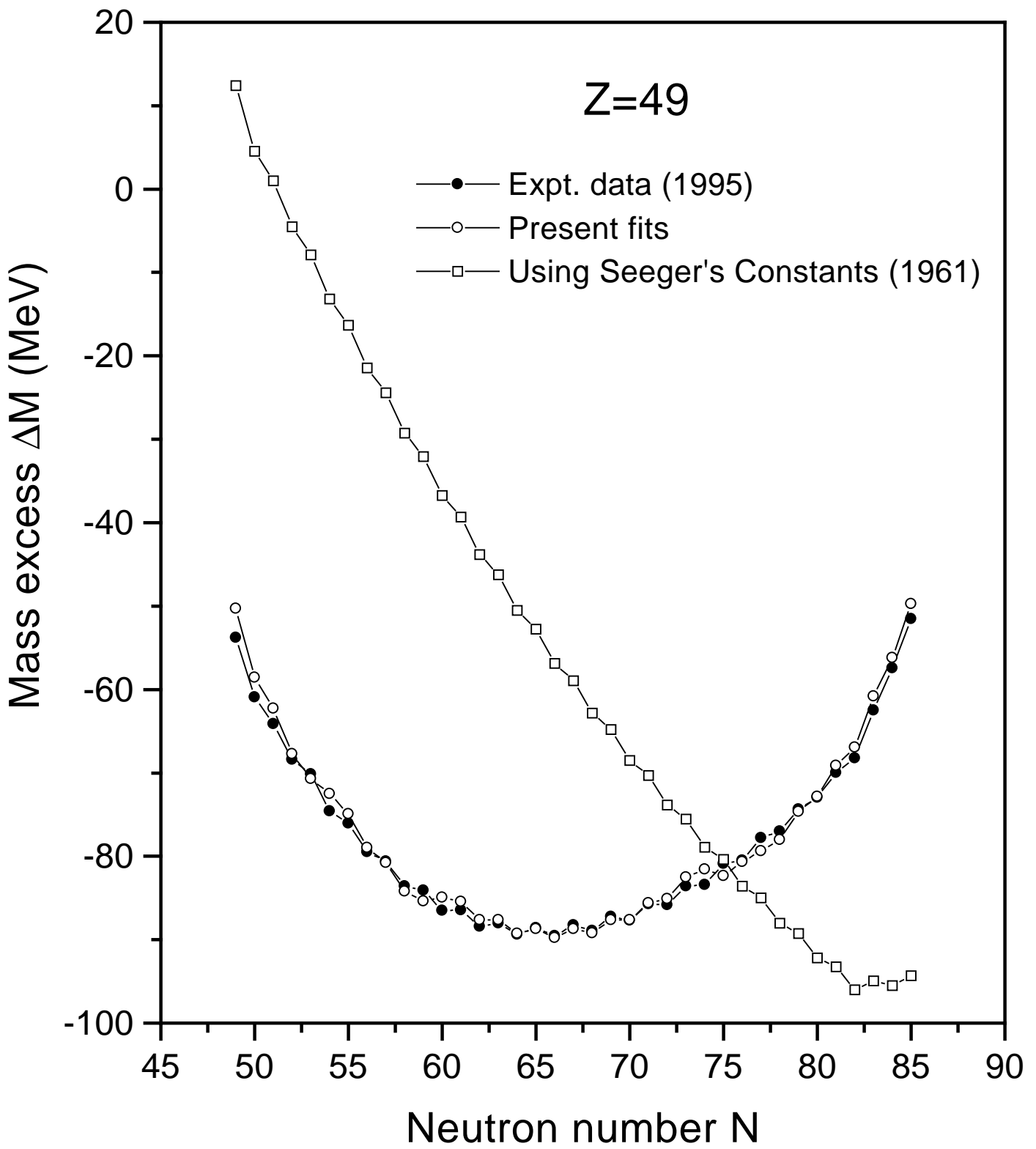


Fig. 2 Balasubramaniam, Kumar, Gupta, Beck and Scheid "Emission of intermediate mass fragments from hot ^{116}Ba"

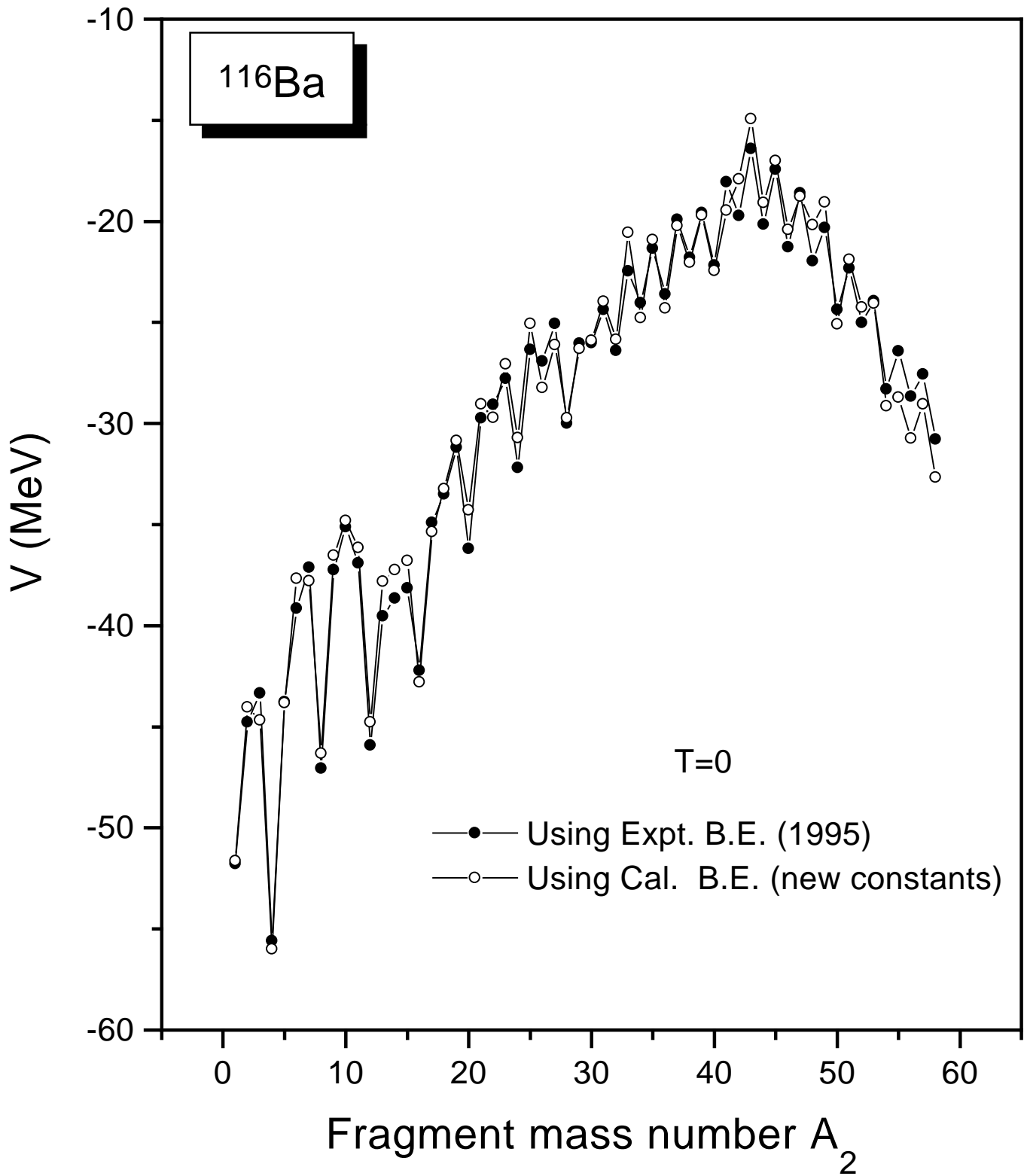


Fig. 3 Balasubramaniam, Kumar, Gupta, Beck and Scheid "Emission of intermediate mass fragments from hot ^{116}Ba"

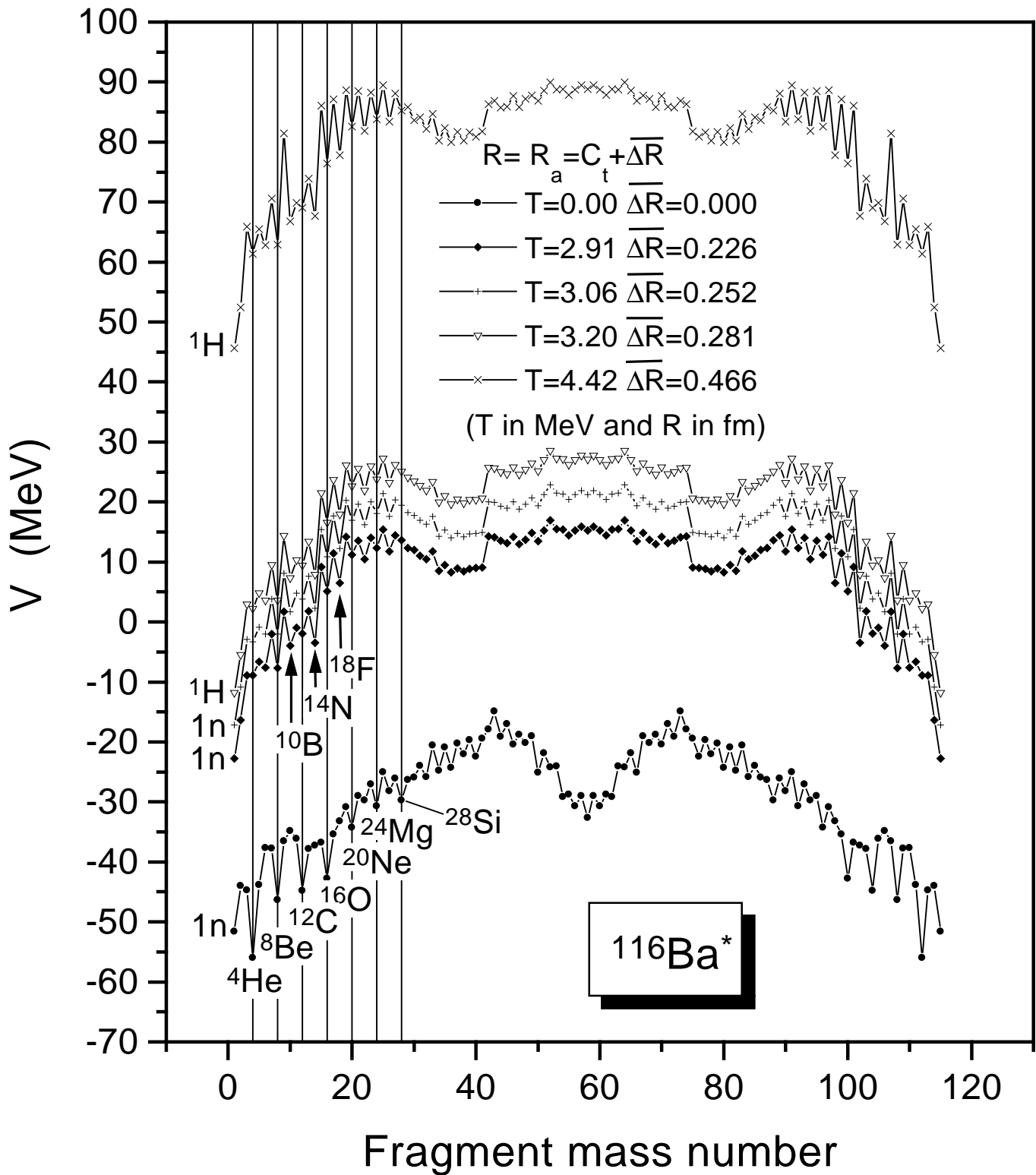


Fig. 4 Balasubramaniam, Kumar, Gupta, Beck and Scheid "Emission of intermediate mass fragments from hot ${}^{116}\text{Ba}$"

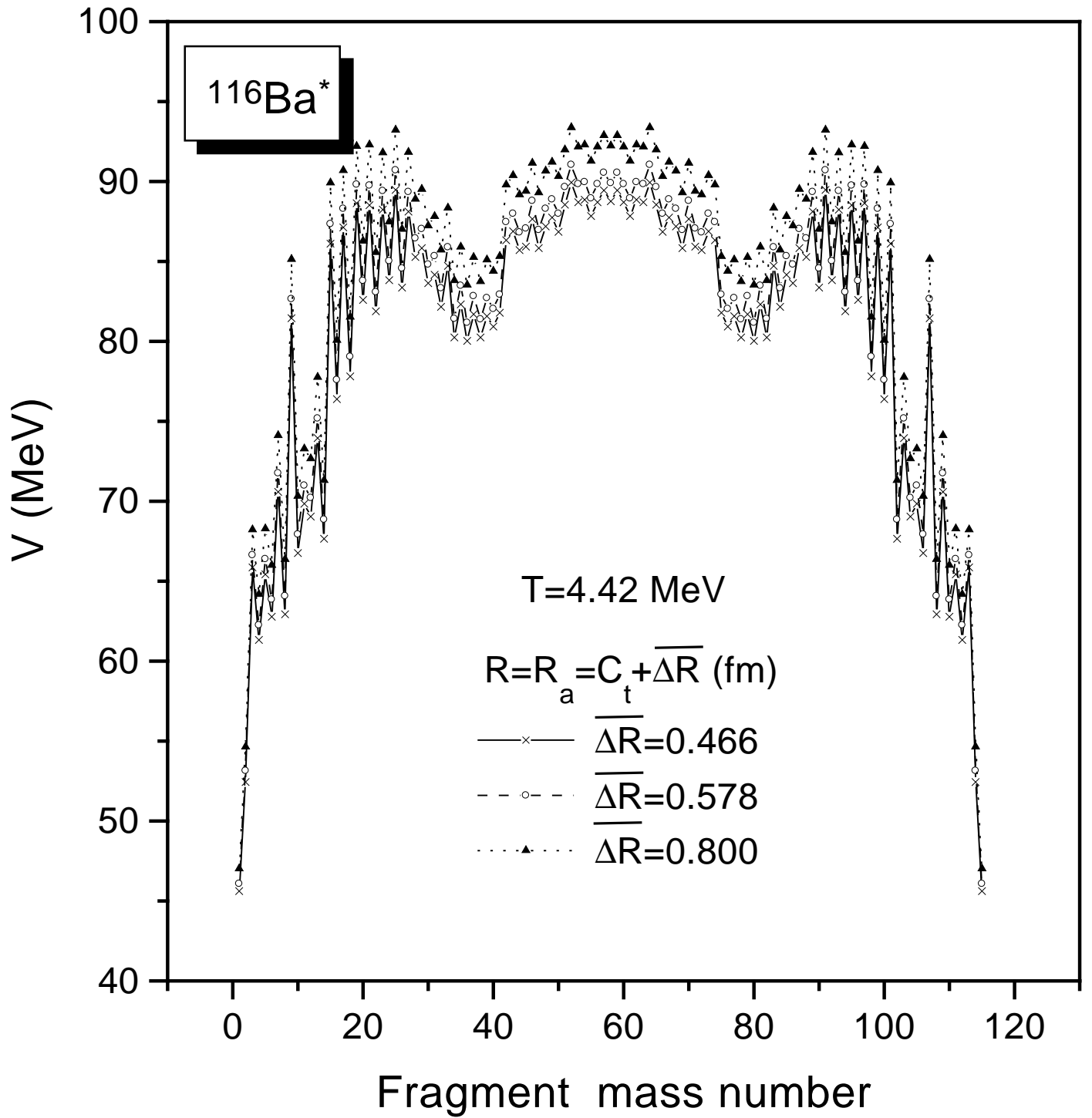


Fig. 5 Balasubramaniam, Kumar, Gupta, Beck and Scheid "Emission of intermediate mass fragments from hot ^{116}Ba"

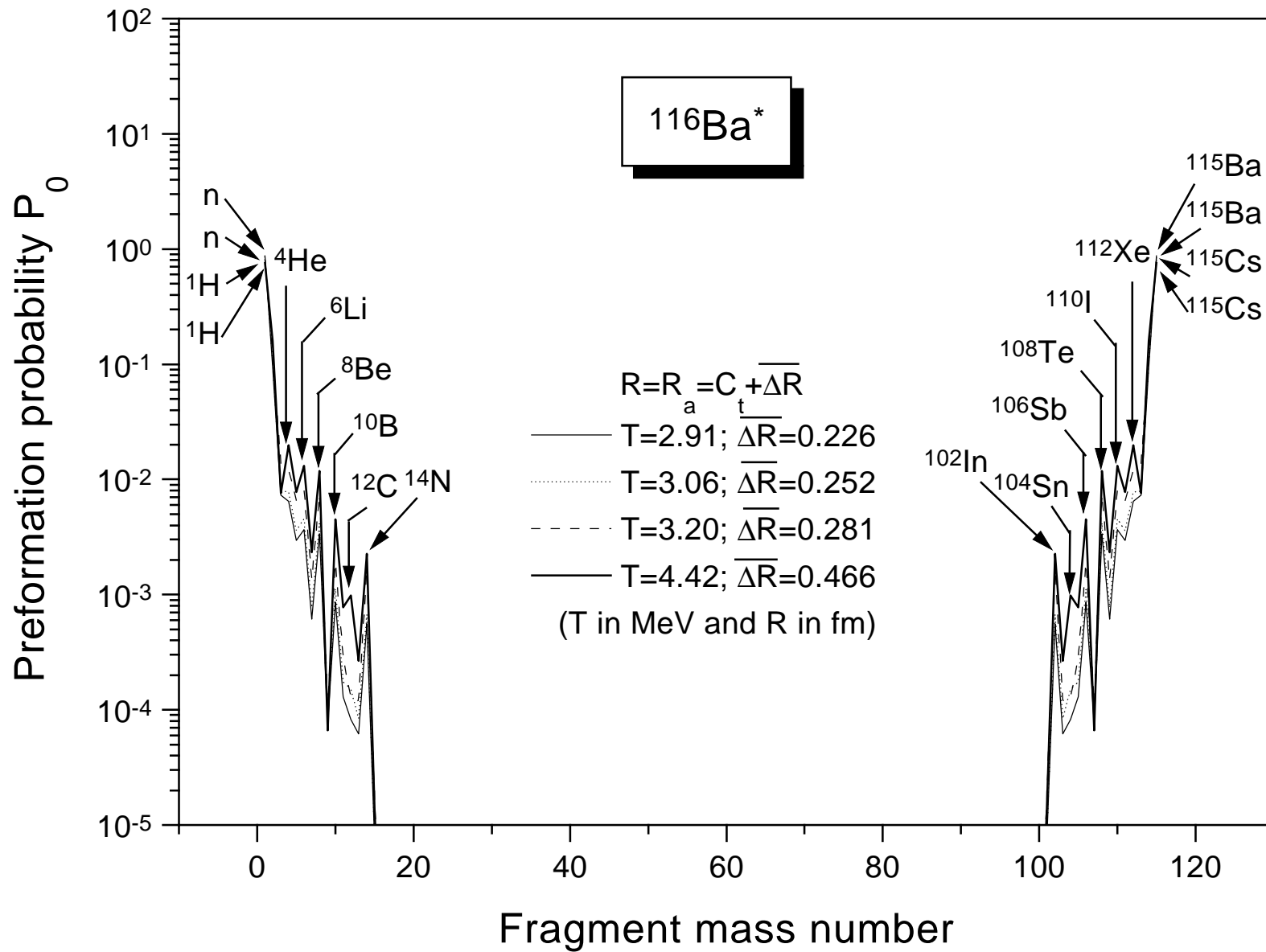


Fig. 6 Balasubramaniam, Kumar, Gupta, Beck and Scheid "Emission of intermediate mass fragments from hot ^{116}Ba"

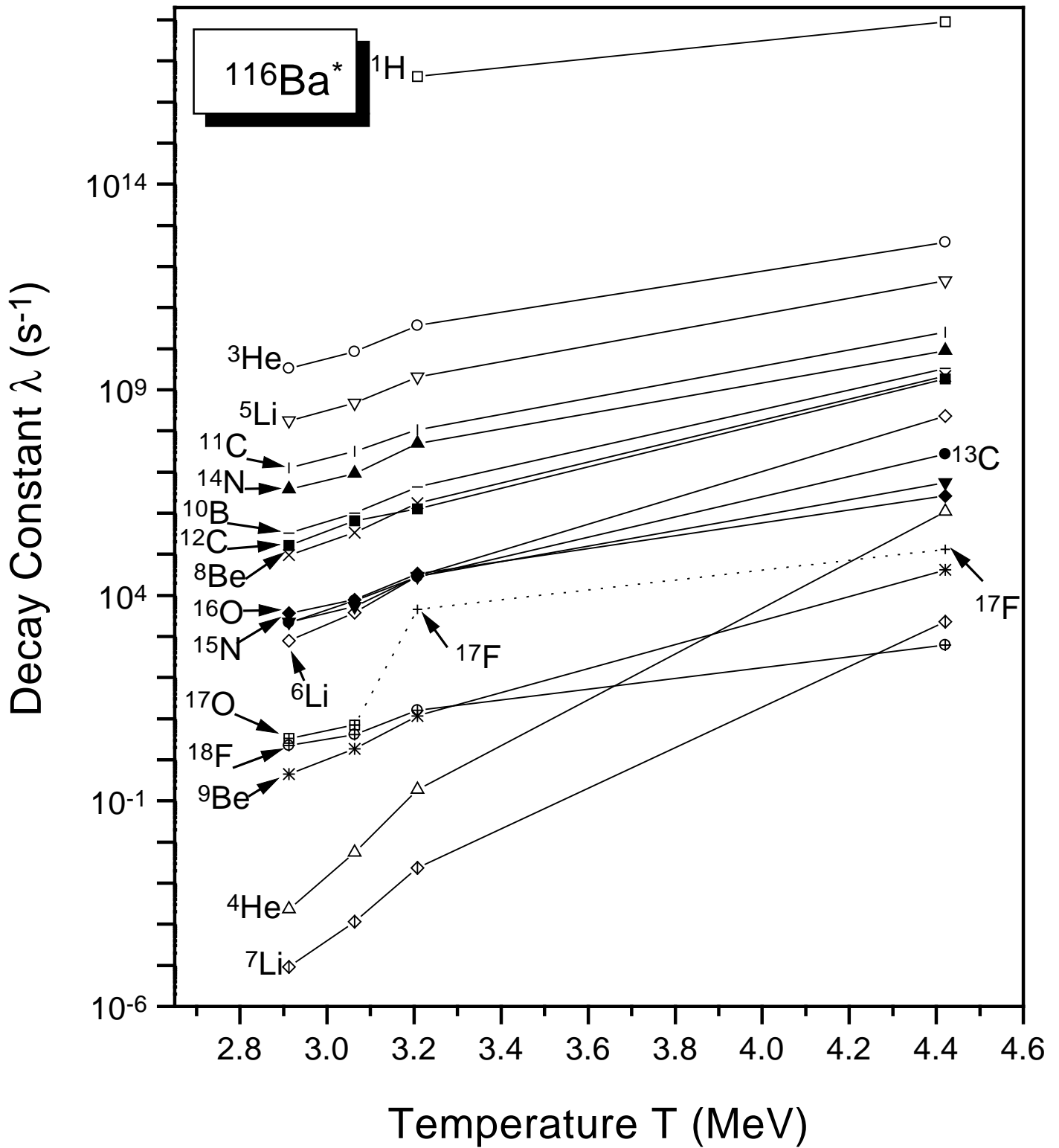


Fig. 7 Balasubramaniam, Kumar, Gupta, Beck and Scheid "Emission of intermediate mass fragments from hot ^{116}Ba"

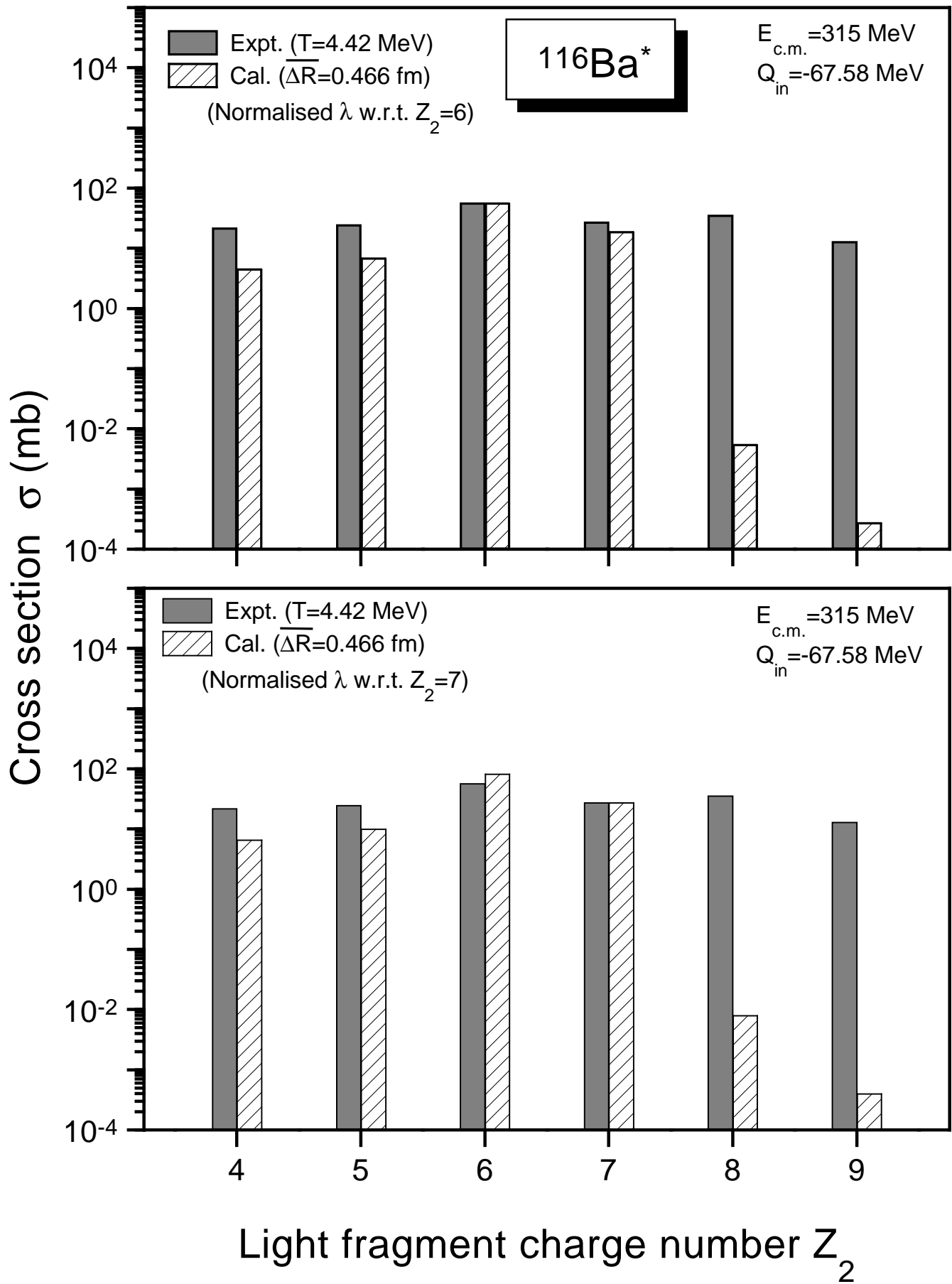


Fig. 8 Balasubramaniam, Kumar, Gupta, Beck and Scheid "Emission of intermediate mass fragments from hot ^{116}Ba"

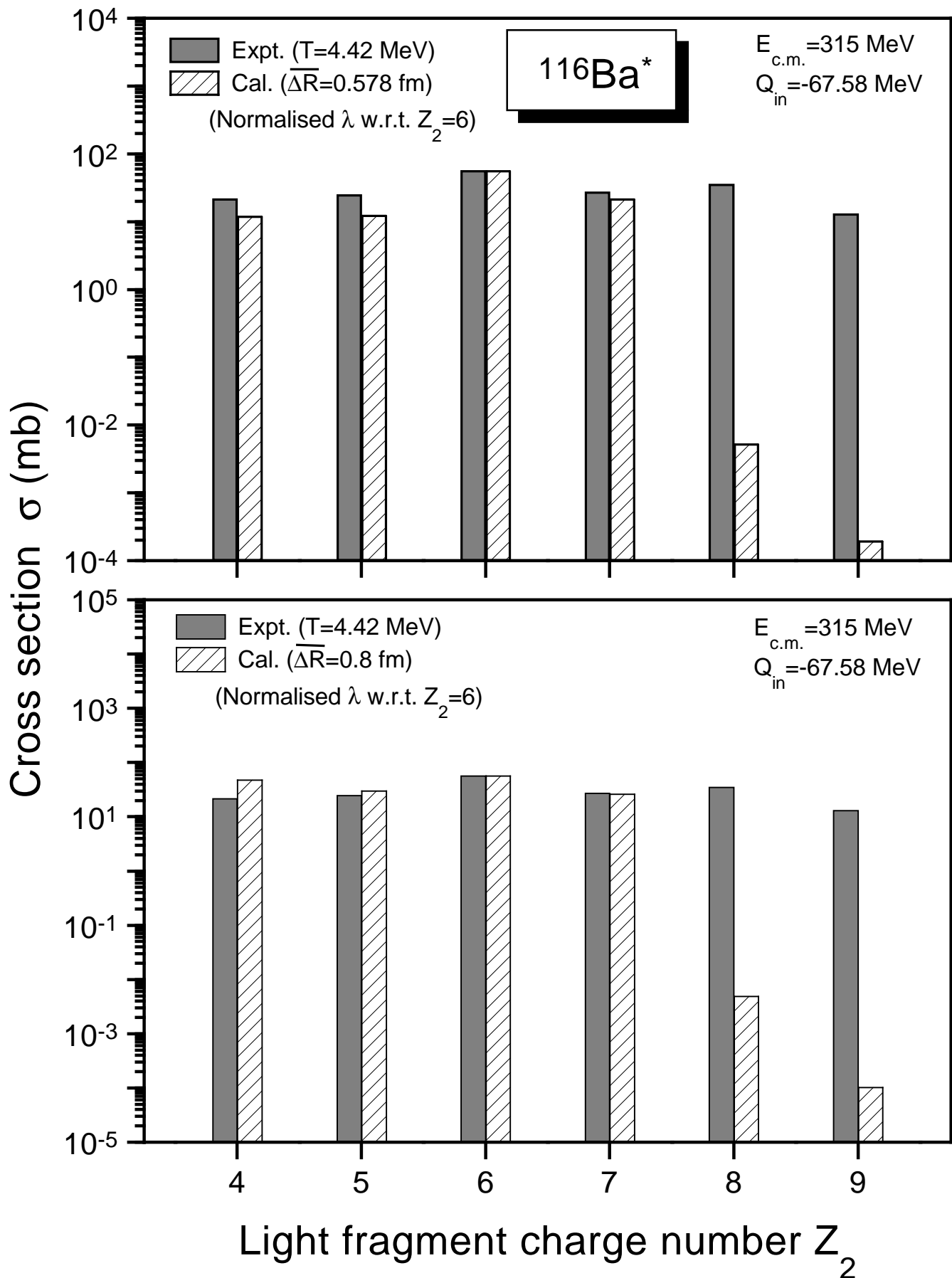


Fig. 9 Balasubramaniam, Kumar, Gupta, Beck and Scheid "Emission of intermediate mass fragments from hot ^{116}Ba"

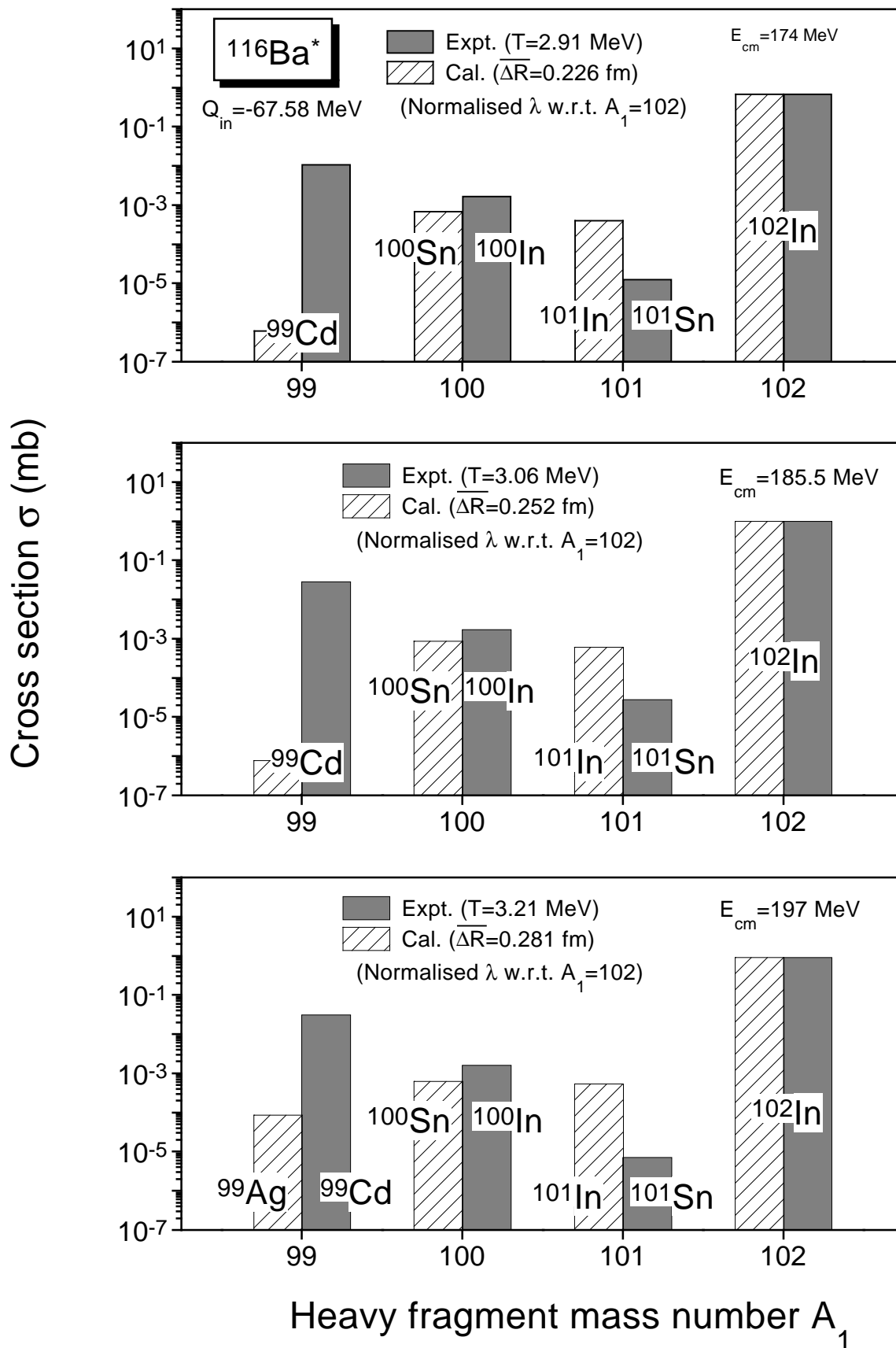


Fig. 10 Balasubramian, Kumar, Gupta, Beck and Scheid "Emission of intermediate mass fragments from hot ^{116}Ba"

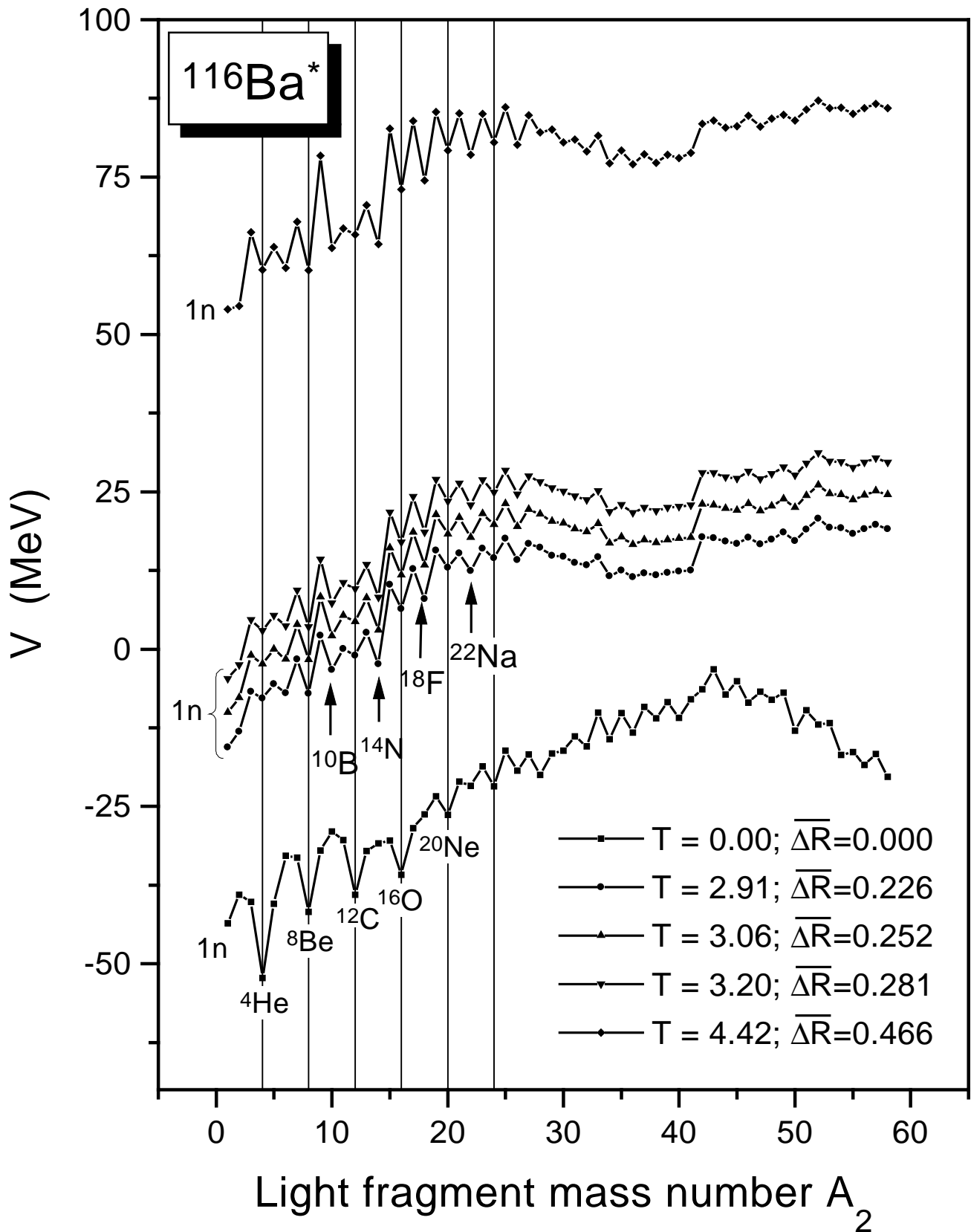


Fig. 11 Balasubramaniam, Kumar, Gupta, Beck and Scheid "Emission of intermediate mass fragments from hot ^{116}Ba"

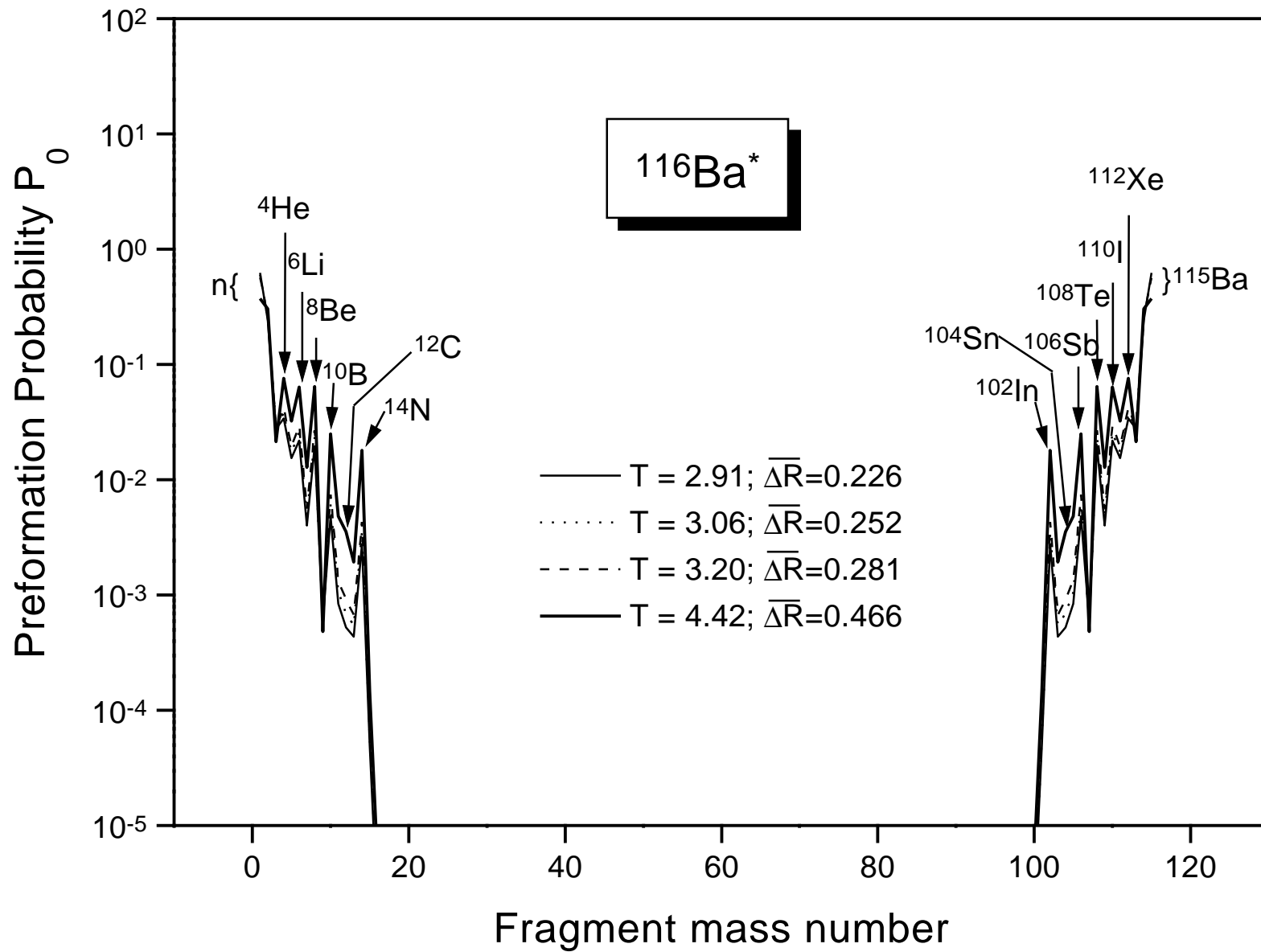


Fig. 12 Balasubramaniam, Kumar, Gupta, Beck and Scheid "Emission of intermediate mass fragments from hot ^{116}Ba"

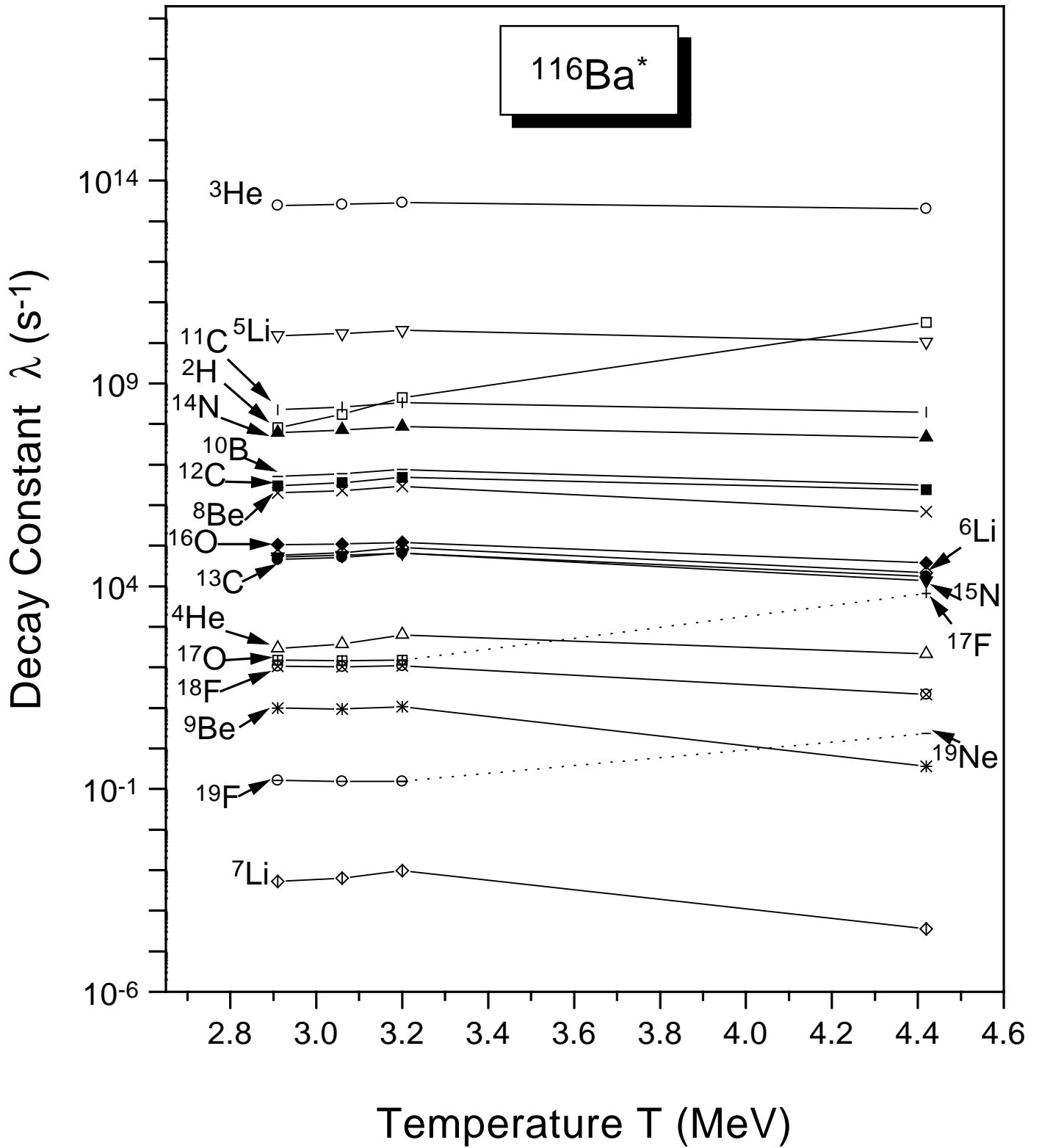


Fig. 13 Balasubramaniam, Kumar, Gupta, Beck and Scheid "Emission of intermediate mass fragments from hot ^{116}Ba"

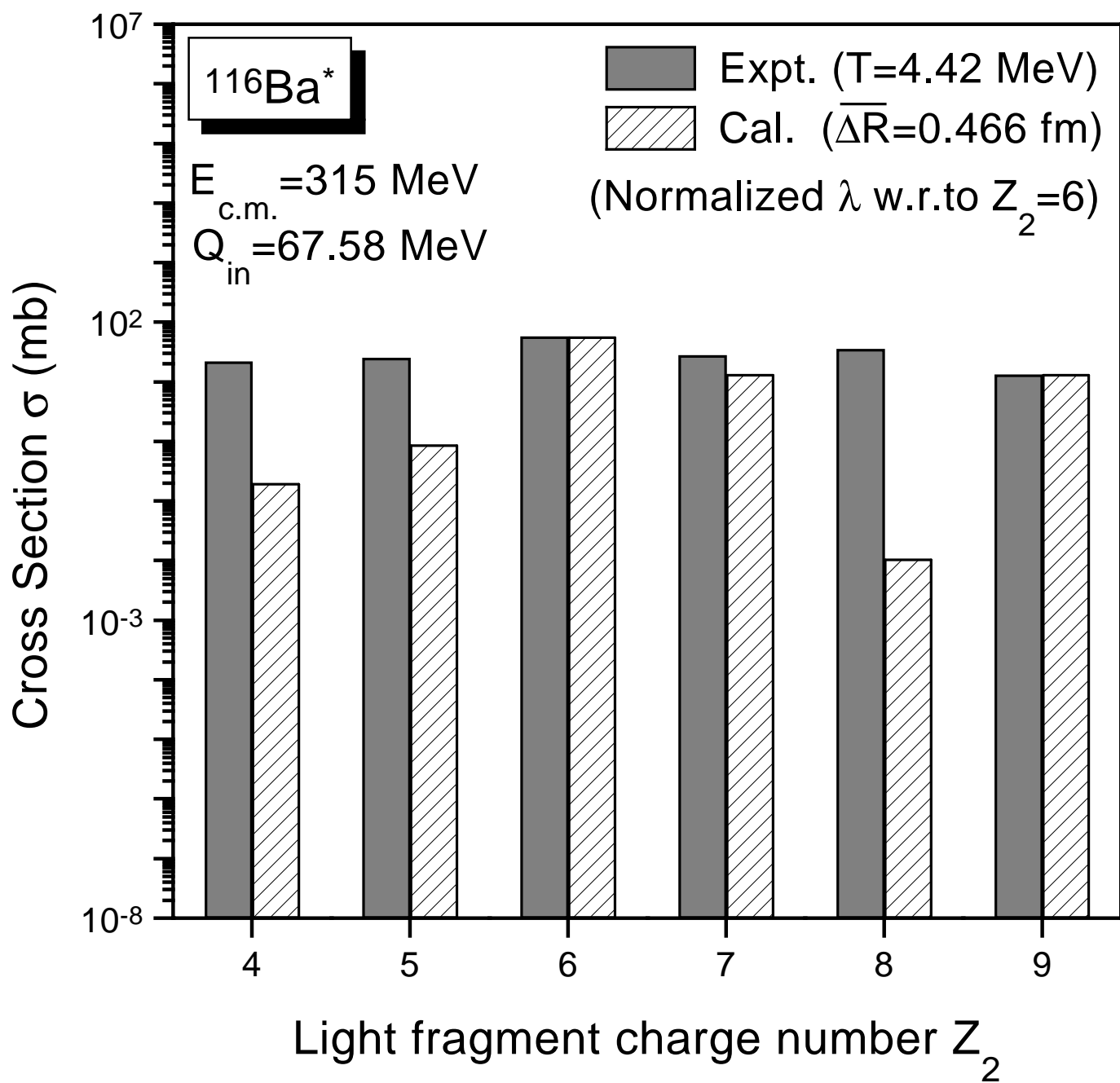


Fig. 14 Balasubramaniam, Kumar, Gupta, Beck and Scheid "Emission of intermediate mass fragments from hot ^{116}Ba"

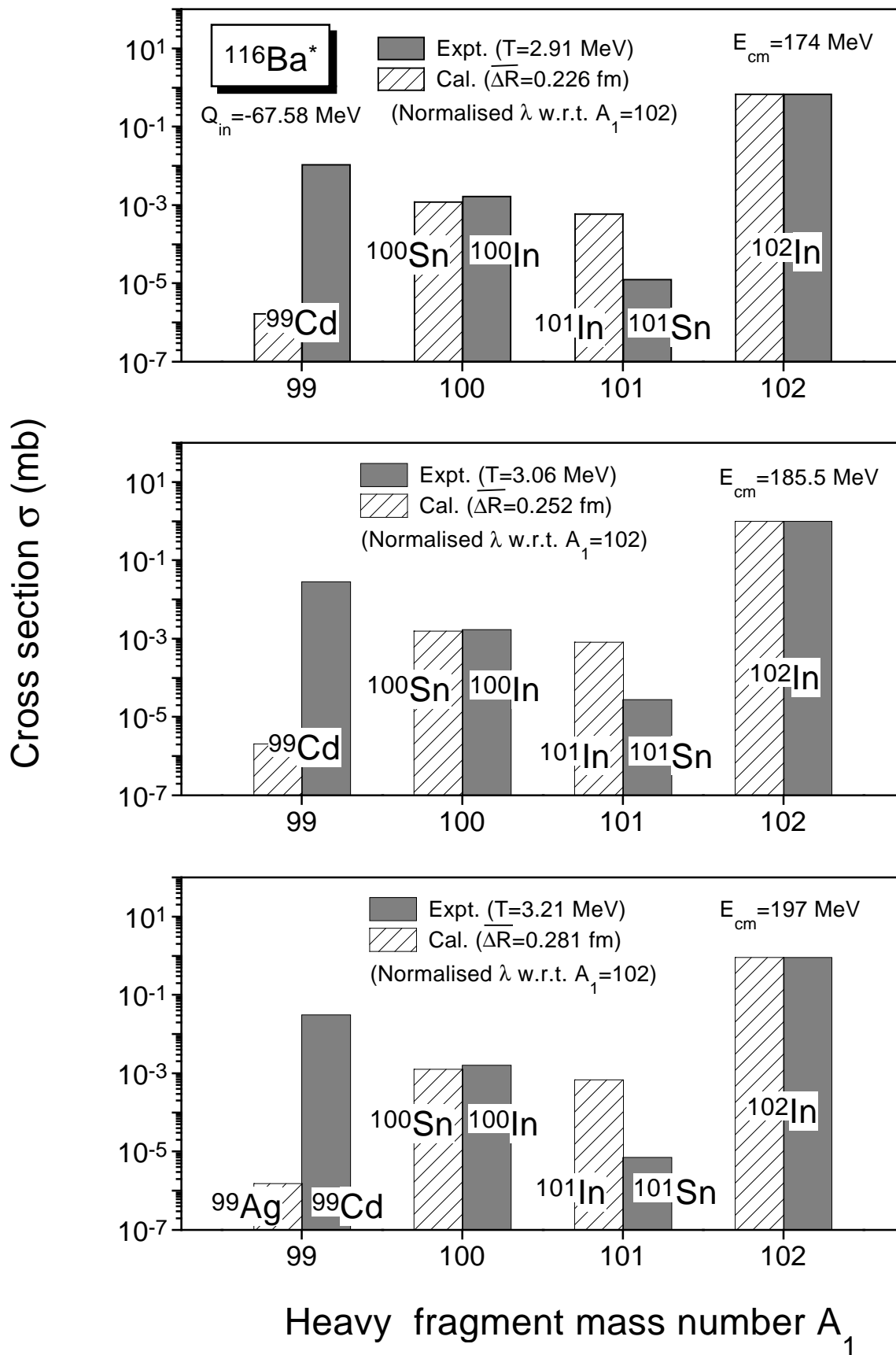


Fig. 15 Balasubramaniam, Kumar, Gupta, Beck and Scheid "Emission of intermediate mass fragments from hot ^{116}Ba"